Separation Control with Nanosecond Pulse Driven Dielectric Barrier Discharge Plasma Actuators

Jesse Little[1]

University of Arizona, Department of Aerospace and Mechanical Engineering, Tucson, AZ, 85721

Keisuke Takashima[2], Munetake Nishihara[3], Igor Adamovich[4] and Mo Samimy[5]

The Ohio State University, Department of Mechanical and Aerospace Engineering, Columbus, OH, 43235

The efficacy of dielectric barrier discharge (DBD) plasmas driven by high voltage (~15 kV) repetitive nanosecond pulses (~100 ns FWHM) for flow separation control is investigated experimentally on an airfoil leading edge up to Re=1x10^6 (62 m/s). Unlike AC-DBDs, the nanosecond pulse driven DBD plasma actuator transfers very little momentum to the neutral air, but generates compression waves similar to localized arc filament plasma actuators. A complex pattern of quasi-planar and spherical compression waves is observed in still air. Measurements suggest that some of these compression waves are generated by discharge filaments that remain fairly reproducible pulse-to-pulse. The device performs as an active trip at high Re pre-stall angles of attack and provides perturbations that generate coherent spanwise vortices at post-stall. These coherent structures entrain freestream momentum thereby reattaching the normally separated flow to the suction surface of the airfoil. Coherent structures are identified at all tested frequencies, but values of F_c^+=4-6 are most effective for control. Such devices which are believed to function through thermal effects could be an alternative to AC-DBD plasmas that rely on momentum addition.

---

[1] Assistant Professor, AIAA Member
[2] Post-Doctoral Researcher, AIAA Member
[3] Post-Doctoral Researcher, AIAA Member
[4] Professor, AIAA Associate Fellow
[5] The Howard D. Winbigler Professor of Engineering, AIAA Fellow, Corresponding Author, samimy.1@osu.edu

Report Documentation Page		Form Approved OMB No. 0704-0188

1. REPORT DATE **2011**	2. REPORT TYPE	3. DATES COVERED **00-00-2011 to 00-00-2011**

4. TITLE AND SUBTITLE	5a. CONTRACT NUMBER
Separation Control with Nanosecond Pulse Driven Dielectric Barrier Discharge Plasma Actuators	5b. GRANT NUMBER
	5c. PROGRAM ELEMENT NUMBER
6. AUTHOR(S)	5d. PROJECT NUMBER
	5e. TASK NUMBER
	5f. WORK UNIT NUMBER

7. PERFORMING ORGANIZATION NAME(S) AND ADDRESS(ES) **Ohio State University,Department of Mechanical Engineering,Columbus,OH,43235**	8. PERFORMING ORGANIZATION REPORT NUMBER

9. SPONSORING/MONITORING AGENCY NAME(S) AND ADDRESS(ES)	10. SPONSOR/MONITOR'S ACRONYM(S)
	11. SPONSOR/MONITOR'S REPORT NUMBER(S)

12. DISTRIBUTION/AVAILABILITY STATEMENT **Approved for public release; distribution unlimited**

13. SUPPLEMENTARY NOTES **accepted for publication in AIAA Journal, 2011**

14. ABSTRACT

15. SUBJECT TERMS

16. SECURITY CLASSIFICATION OF:			17. LIMITATION OF ABSTRACT	18. NUMBER OF PAGES	19a. NAME OF RESPONSIBLE PERSON
a. REPORT **unclassified**	b. ABSTRACT **unclassified**	c. THIS PAGE **unclassified**	**Same as Report (SAR)**	**42**	

Nomenclature

a	=	local speed of sound
c	=	model chord, 25.4 cm
d	=	plasma filament diameter
f	=	frequency
x_{sep}	=	separation length scale
U	=	instantaneous streamwise velocity
$\overline{U}$	=	ensemble-averaged streamwise velocity
$\tilde{U}$	=	phase-averaged streamwise velocity
U_∞	=	freestream velocity
V	=	instantaneous streamwise velocity
$\overline{V}$	=	ensemble-averaged normal velocity
$\tilde{V}$	=	phase-averaged normal velocity
x	=	streamwise coordinate
y	=	vertical coordinate
α	=	angle of attack in degrees
ρ	=	air density
τ_{rise}	=	pulse rise time
$\tau_{acoustic}$	=	acoustic time scale
λ	=	plasma wavelength
λ_{ci}	=	swirling strength
λ_{ci}^{*}	=	normalized swirling strength, $\lambda_{ci}c/U_\infty$
v	=	kinematic viscosity
C_D	=	drag coefficient
C_L	=	sectional lift coefficient
c_P	=	fluctuating pressure coefficient
C_P	=	pressure coefficient

F_c^+ =   reduced frequency based on model chord, fc/U_∞

Re =   chord based Reynolds number, $U_\infty c/v$

Φ =   phase

Ω =   spanwise component of vorticity

Ω^* =   normalized spanwise vorticity, $\Omega c/U_\infty$

I. Introduction

Flow over solid bodies is retarded near the surface due to viscous effects which give rise to a boundary layer. Often the near wall fluid must also negotiate an adverse pressure gradient and/or geometric aberration. Flow separation occurs when the momentum in the boundary layer is insufficient to overcome these impediments. This is marked by a thickening of the rotational region of fluid near the surface and an increase in the wall normal velocity component. Boundary layer separation is synonymous with substantial energy losses and minimizing its occurrence is one of the primary design objectives for aerodynamic and hydrodynamic systems.

A common platform for investigating separation control is the airfoil at high angle of attack. This system produces maximum lift near the angle at which separation occurs from the leading edge. Slight excursions to higher angles can result in unrecoverable stall. Transport aircraft often combat this problem using passive control devices in the form of segmented leading edge slats that deploy during takeoff and landing to promote mixing between high momentum fluid on the pressure surface with low momentum fluid on the suction surface. These passive geometric modifications are effective for augmenting lift, but create significant increases in mechanical complexity, manufacturing cost, weight and parasitic drag even when stowed during cruise.

Active flow control in the form of localized periodic excitation has been used to impart global changes to separated flow fields.[1] This is often accomplished by adding spanwise slots to the aerodynamic surface near separation locations. Periodic excitation, usually in the form of momentum, is delivered through the slots to manipulate natural flow instabilities in an effort to prevent or reattach separated flows. The optimal dimensionless frequency, $F^+=fx_{sep}/U_\infty$, for controlling separation using periodic excitation is on the order of unity where f, x_{sep} and U_∞ are the forcing frequency, separation length scale and freestream velocity respectively.[2] Periodic excitation can

American Institute of Aeronautics and Astronautics

be accomplished through a variety of mechanisms, but piezoelectric, electromagnetic or electrostatic devices are often employed. In all of these cases, an electromechanical driver creates the oscillatory flow used for excitation. These devices are controlled through electrical signals and, compared to passive control, offer a significant reduction in weight, mechanical complexity and parasitic drag. Unfortunately, they possess limited bandwidth and are subject to mechanical failure because the electromechanical driver is usually operated at resonance to produce the large amplitude perturbations necessary at practical flight speeds. Even when operated in this fashion, it is difficult to meet amplitude requirements especially for cruise conditions since the required actuator momentum scales roughly with dynamic pressure.[1]

Flow control with plasma actuation is appealing because these devices are surface mounted, lack mechanical parts and require relatively low power. Dielectric Barrier Discharge (DBD) plasma actuators driven by AC waveforms (AC-DBD) are the most popular.[3] They have been demonstrated for airfoil leading edge separation control at freestream velocities up to 60 m/s ($Re \approx 10^6$).[4] The control mechanism for AC-DBD plasma actuators arises from an electrohydrodynamic (EHD) effect (i.e. Coulomb force interaction). The signature of this mechanism is generation of a low speed (usually <10 m/s) near wall jet in quiescent air due to interaction between the charged species in the plasma and neutral particles near the surface. The technology continues to improve through optimization of a single actuator, the use of multiple actuators/electrodes and sliding discharges that rely on additional DC potential.[5-8] The common goal in these cases is to increase the momentum production of the device.

Early reports suggest DBD plasma actuators driven by a different type of waveform could be an alternative. The construction of the device is analogous to the AC-DBD, but the discharge is driven by repetitive nanosecond duration pulses (FWHM≈5-100 ns)). We will refer to this type of actuation as a repetitive nanosecond pulse discharge or "NS-DBD" throughout the paper. DBD plasma created using these waveforms has shown control authority for leading edge airfoil separation control up to Mach 0.85,[9] but many questions about the underlying flow physics remain unanswered. It should be noted that such waveforms have also been used in combination with AC and DC bias voltage, but to the authors knowledge these have not been tested in flow control studies.[10,11]

The mechanism by which NS-DBD plasmas produce control is believed to be substantially different from the AC discharge. The NS-DBD produces very low velocity in the neutral species. Instead, a thermal effect (i.e. Joule heating) that generates a local compression wave is believed to provide the control mechanism. Indeed, compression waves generated in quiescent air by localized heating of the near surface gas layer have been detected in both

American Institute of Aeronautics and Astronautics

modeling and experiment.[9,12] This scenario is well-established for localized arc filament plasma actuators (LAFPAs) that are effective for controlling high Reynolds number and high-speed (subsonic/supersonic, cold/hot) jets in both experiments[13-15] and computations.[16] Like many flow control studies, the main idea of the LAFPA approach is to force the flow at a frequency approaching one of the flow instabilities, thereby triggering subsequent growth of seeded perturbation and their rollup into flow structures. In high speed flow this requires both high amplitude and high bandwidth to realize performance goals across various flight regimes. Studies of flow control using LAFPAs in atmospheric pressure cold and hot jets (M=0.9-2.0) demonstrate significant localized heating and repetitive compression wave formation which excite flow instabilities that alter dynamics of large-scale coherent structures thereby achieving noise reduction and mixing enhancement. In fact, these are the only devices that have shown this capability at high speeds. This has been accomplished with relatively low actuator power, (~10 W per actuator), at forcing frequencies near the jet column (preferred mode) instability frequency. Thus, the main benefit for flow control with thermal perturbations seems to be their use at high speeds where it is difficult for momentum based devices to reliably or efficiently produce sufficient momentum for control authority. It should be noted that compared to the EHD effect, the effect of Joule heating in surface DBD actuators driven by AC voltage waveforms appears insignificant.[17-19]

This paper describes the development and application of nanosecond pulse driven DBD plasma actuators for controlling flow separation from an airfoil leading edge. The NS-DBD plasma actuator is characterized using electrical measurements and optical techniques in quiescent air. Control authority is demonstrated on an airfoil leading edge up to $Re=1\mathrm{x}10^6$ (62 m/s) using static pressure and PIV measurements. Results show the NS-DBD can perform as an active boundary layer trip or generate coherent spanwise vortices that are widely associated with controlling separation in a variety of flow systems.[1] The employed control mechanism (active trip or coherent vortex) is dependent on the Reynolds number and angle of attack. The generation of large-scale structures via thermal perturbations is in agreement with experiments using LAFPAs on hot and cold high speed high Re jets. This suggests that the mechanisms of flow control for both types of actuators may be similar.

II. Experimental Facilities and Techniques

A. NS-DBD Plasma Actuator

The DBD plasma actuators in this work are composed of two copper tape electrodes separated by Kapton tape dielectric arranged in an asymmetric fashion (Figure 1). There is a slight overlap between the electrodes to encourage uniform plasma generation. The covered ground electrode is 12.7 mm (½ inch) wide and the exposed high voltage electrode is 6.35 mm (¼ in) wide. Both electrodes have thickness of 0.09 mm (3.5 mil). The dielectric barrier is composed of 3 layers of Kapton tape. Each layer has thickness of 0.09 mm (3.5 mil) and dielectric strength of 10 kV. Each layer of Kapton tape has a 0.04 mm (1.5 mil) layer of silicone adhesive such that the actual Kapton thickness for each tape layer is only 0.05 mm (2 mil). The total thicknesses of the dielectric and the device as a whole are 0.27 mm (10.5 mil) and 0.44 mm (17.5 mil) respectively. The actuator construction has been determined based on previous studies of AC-DBD plasma and has not been optimized for NS-DBD purposes.[20,21] The actuator is directly applied to the substrate in all cases.
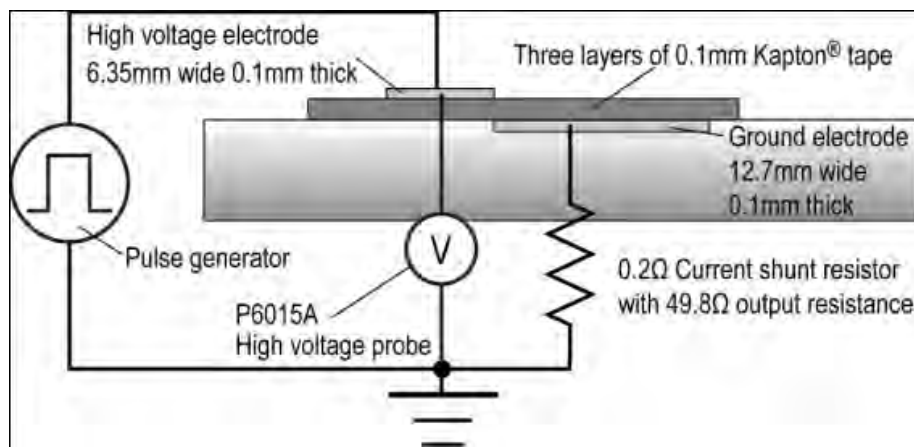

Figure 1. DBD Plasma actuator schematic with connections for electrical measurements

Two surface DBD plasma setups have been used for actuator characterization. The first setup, shown in Figure 1, is mounted on a flat dielectric surface and used for nanosecond discharge pulse energy and induced flow measurements. The second setup, used for schlieren imaging, employed an actuator with the same electrode geometry mounted on a 5 cm diameter cylinder. In these measurements, the actuator length (into the page) is fixed at 30 cm. The cylinder is chosen to simplify alignment of the schlieren diagnostic. Figure 2 shows a photograph of the second actuator, with the repetitive nanosecond pulse discharge in operation. In all cases, the repetitive nanosecond pulse voltage waveform for the surface DBD discharge is generated by high-voltage magnetic compression type

pulsed power supplies, custom designed and built at The Ohio State University. Briefly, these power supplies generate high voltage pulses (peak voltage up to 20 kV, pulse duration 50-100 nsec FWHM), at a continuous pulse repetition rate of up to 3 kHz, and pulse energy of up to 100 mJ/pulse. Note that there is no lower bound on the repetition frequency and no low frequency burst or amplitude modulation is performed in this work. Both the peak voltage and the pulse energy coupled to the load are strongly load-dependent. The pulse waveform is transmitted to the DBD actuator load via a collinear pair transmission line up to 1.5 m long.
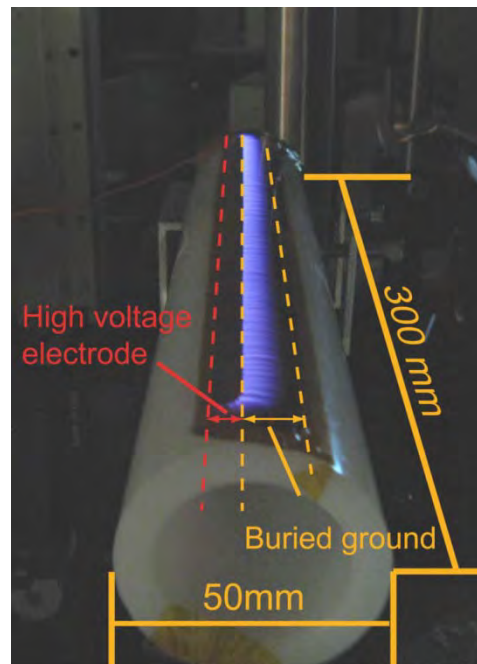

Figure 2. Photograph of a NS-DBD actuator mounted on a cylinder in operation

B. Plasma Diagnostics

Pulse voltage and current have been measured using a Tektronix P6015 high voltage probe, a custom made current shunt probe, and a Tektronix TDS2024 oscilloscope. Both are measured at the end of the transmission line, where the transmission line cables are connected to the load. The current probe uses five resistors of 1 Ω each, with the total resistance of 0.2 Ω, arranged radially to minimize residual inductance. The impedance of the current probe is set at 50 Ω by adding a 49.8 Ω resistor. A schematic of the setup is shown in Figure 1. For termination of the current probe signal, a 50 Ω feed-through terminator resistor is used at the oscilloscope. This reduced multiple reflections of the current probe signal from the oscilloscope and from the current probe. The stray phase shift

between the high voltage probe signal and the current probe signal is determined by reducing to zero the integral of the product of voltage and current at the conditions when the pulse voltage is low (a few hundred Volts) (i.e. when breakdown between the actuator electrodes is not produced).[22]

Compression waves generated by the nanosecond pulse discharge in the DBD actuator are detected using a custom-build phase-locked schlieren system. The light source is a 5 W green light emitting diode (LED) controlled by a custom made drive circuit, which can operate both in continuous emission and pulsed mode. To enhance the sensitivity, a short focal length plano-convex lens is used to focus the LED light at the knife edge. The schlieren images are acquired by a Thorlab DCC1545 CMOS camera. To discriminate stray UV/visible emission from the plasma, a green dichroic filter (90% band pass transmission at 510-570 nm for 0° angle of incidence) is placed in front of the camera. The maximum transmission wavelength is varied by rotating the filter. The LED pulse duration is set at 300 ns which gives the required MHz time resolution and high signal to noise ratio necessary for resolving the generated compression waves. The LED is operated in a repetitively pulsed mode at the same pulse repetition rate as the nanosecond pulse discharge in the DBD actuator (1 kHz). The LED drive circuit is synchronized with the pulsed plasma generator with a certain delay time and phase-locked schlieren images are averaged over 150 to 220 discharge pulses. A reference time is defined as the moment when the discharge current reaches 50% of its peak value. The delay time between this reference and the LED emission pulse is approximately 3 μsec. The pulsed plasma generator jitter is approximately 50-100 nsec and with the overall timing uncertainty of ±200 nsec the uncertainty of the wave front position becomes 0.07 mm.

C. Wind Tunnel Facility and Airfoil Model

A recirculating wind tunnel with an optically accessible 61 x 61 x 122 cm^3 (2 x 2 x 4 ft^3) closed test section serves as the test bed. Test sections walls are constructed of 25.4 mm (1 in) thick super abrasion resistant acrylic. Each side wall is fitted with a 30.5 cm (12 in) diameter port that is located 30.5 cm (12 in) from the test section floor and 61 cm (24 in) downstream of the test section entrance. Air flow in the tunnel is continuously variable from 3-90 m/s (10-300 ft/s). Flow conditioning upstream of the test section includes a hexagonal cell aluminum honeycomb while high porosity stainless steel screens are mounted downstream of the test section as a safety catch. Four high efficiency turning cascades fabricated of galvanized steel are installed in each of the four tunnel elbows. This assembly results in freestream turbulence levels of ~0.25% near the test section inlet. The tunnel is also equipped

with a commercial aluminum fin/copper tube, double row heat exchanger with set point controller and electronic modulating valve. This arrangement allows the tunnel freestream operating temperature to be maintained within 1°C from the ambient when supplied a sufficient source of cooling water (max 189 lpm (50 gpm)).

The airfoil is a simplified high-lift version of the NASA Energy Efficient Transport (EET) with chord length of 25.4 cm (10 in) and span of 61 cm (2 ft). It was originally designed for studies of separation control over a deflected flap at low angle of attack.[20,21] The current work examines separation from the leading edge at high angle of attack with no flap deflection. The model is constructed of a nylon compound (Duraform GF) and has been fabricated using selective laser sintering (SLS) technology. Angle of attack settings are done manually using a protractor on the side wall. Forty five static pressure taps are staggered around the test section centerline. The airfoil is mounted across the span of the tunnel and supported by 12 inch diameter wall plugs on either side. Maximum blockage in the current study is ~12% and occurs at 16° angle of attack. No blockage or wall corrections have been employed. While it is quite challenging, future studies should investigate the effect of blockage on active flow control in general. To the author's knowledge this has not been addressed in the literature. Significant studies on active flow control with zero net mass flux actuators have been completed for a more complex version of this airfoil.[23-28]

D. Flow Diagnostics

Measurements of static pressure from taps on the model surface are acquired using Scanivalve digital pressure sensor arrays (DSA-3217). Subsequent values of sectional C_P and C_L are averaged over 50 samples acquired at 1 Hz. A flush mounted Kulite pressure transducer (XCQ-080-25A) in the model at x/c=0.40 is powered using an in-house constructed signal conditioner that amplifies output by 1000. A separate Kemo unit is employed for low-pass filtering at 25 kHz. The resulting pressure traces are sampled simultaneously at 50 kHz using a National Instruments PCI-6143 data acquisition board. Average spectra are calculated from 50 blocks of 8192 samples which results in a frequency resolution of approximately 6 Hz. A Hanning window function is applied to each block.

Two-component particle image velocimetry (PIV) is used to obtain quantitative measurements of the velocity fields over the airfoil and the DBD actuator on a flat plate in still air. Images are acquired and processed using a LaVision PIV system. Nominally submicron olive oil seed particles are introduced upstream of the test section contraction using a 6-jet atomizer. A dual-head Spectra Physics PIV-400 Nd:YAG laser is used in conjunction with spherical and cylindrical lenses to form a thin light sheet that allows PIV measurements. The time separation

between laser pulses used for particle scattering is set according to the flow velocity, camera magnification and correlation window size. Two images corresponding to the pulses from each laser head are acquired by a LaVision 14 bit 2048 by 2048 pixel Imager Pro-X CCD camera equipped with a Nikon Nikkor 50 mm f/1.2 lens. Flat plate PIV data are acquired using an additional 2x teleconvertor to increase spatial resolution. For each image pair, subregions are cross-correlated using decreasing window size (64^2-32^2 pixel^2) multi-pass processing with 50% overlap. The resulting velocity fields are post-processed to remove spurious vectors using an allowable vector range and median filter. Removed vectors are replaced using an interpolation scheme based on the average of neighboring vectors. A 3x3 Gaussian smoothing filter is also applied to the calculated velocity fields. The PIV data are sampled at 10 Hz. Ensemble-averaged statistics for the airfoil and actuator characterization are calculated from 750 and 500 instantaneous velocity fields, respectively. Convergence calculations show these values are more than sufficient for the data presented here.

Phase-locked PIV data are acquired using the programmable timing unit of the LaVision system. The acquisition is synced with the frequency of the actuation signal. Velocity fields at four phases of the actuator frequency are investigated by stepping through the forcing period using time delays. The resulting phase-locked data sets are averaged over 100 images at each phase which convergence calculations show are sufficient for resolving the primary features of the average flow fields (i.e. coherent structures). Phase-locked PIV data is acquired at 5 Hz. The spatial resolutions of PIV data for the airfoil and flat plate data sets are approximately 2.4 and 0.2 mm, respectively. Near surface measurements for the flat plate data sets are obtained within 0.3 mm of the substrate.

Full-scale accuracy for measurements of instantaneous velocity is 1.7% for actuator characterization and 0.9% in the case of the airfoil. This is calculated by assuming negligible laser timing errors and a correlation peak estimation error of 0.1 pixels. The error is smaller in the airfoil case due to better choices of time separation between laser pulses due to the a priori knowledge of maximum velocities in the freestream flow. The uncertainties in measurements of mean velocity are calculated using 95% confidence intervals.[29] This results in relative error of 4-6% for actuator characterization and 2-3% in the airfoil case. The value for the actuator in still air case is estimated using the average standard deviation and average velocity in the near wall profiles which gives a more representative estimate than the maximum velocity. The uncertainty in the airfoil case is estimated using the maximum standard deviation in the turbulent wake and the freestream velocity. A range of values that encompasses all the flow fields surveyed is provided in the interest of brevity. The 95% confidence interval for C_P measurements is smaller than the

presented symbol size. The repeatability of the results is primarily determined by the accuracy with which the actuator can be constructed and adhered to the surface. We estimate this as less than 2 mm.

E. Test Conditions

Leading edge separation control studies have been performed at primarily Re=0.75 x 10^6 (45 m/sec) and 1 x 10^6 (62 m/sec) with no flap deflection. Tests are limited by the structural fidelity of the airfoil model which was not specifically designed for high Re, high angle of attack studies. In this work, the term "baseline" corresponds to test cases where an actuator is installed on the surface with no plasma generation. For all airfoil measurements, data is acquired by establishing a separated flow baseline condition then energizing the actuator. For repeated samples of different forcing cases the baseline separated condition is reestablished between consecutive control cases to eliminate hysteresis effects.

III. Actuator Characterization

A. Electrical Measurements

Figure 3a shows representative discharge pulse voltage and current traces measured on a 30 cm long DBD actuator. Figure 3b plots instantaneous power and time-resolved pulse energy coupled to the load at these conditions. During these measurements, the pulse repetition rate is fixed at 10 Hz to exclude effects of actuator and pulse generator heating on the coupled pulse energy. The peak voltage and current are approximately 16 kV and 50 A, respectively. Steady state energy (13 mJ/pulse) is realized approximately 150 ns after the beginning of the pulse. Peak power of up to 600 kW is generated due to the short pulse width, but the energy is less than 1 mJ/pulse/cm for all actuator lengths surveyed.[22] For the frequencies considered in this work (<3 kHz), this corresponds to time average power of <3 W/cm. The actuator length has an effect on these values, but scaling to 1.5 m has been accomplished by simply increasing the DC voltage applied to the pulse generator.[22] Note that the minimum pulse rise and fall time achieved in a 30 cm long actuator is approximately 40 nsec, which corresponds to a wavelength of $\lambda \approx 24$ m. Therefore at the present conditions, the nanosecond pulse DBD load can be considered as a lumped parameter circuit since the actuator length is much shorter than $\lambda/4$. Provided control authority is realized, this slower rise time is advantageous in practice because it permits the use of longer actuators. At conditions where the

length of the pulse is comparable to actuator length, nonuniform potential distribution along the electrodes becomes problematic.[30]
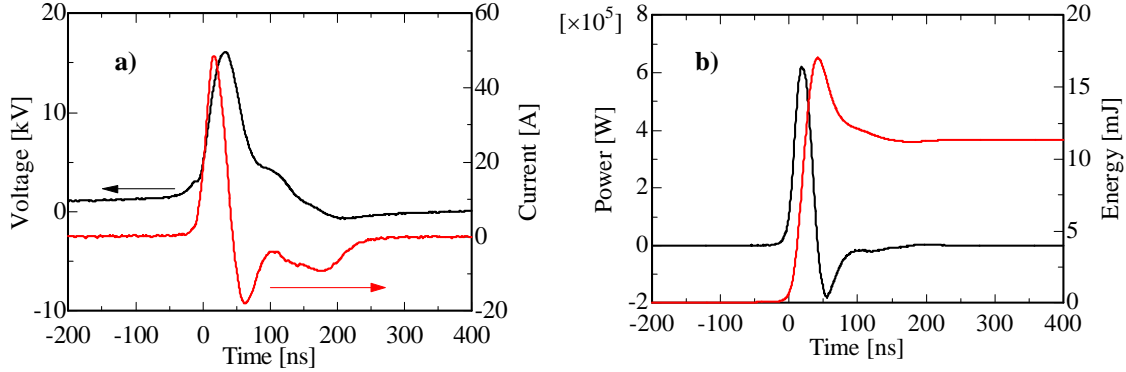

Figure 3. Voltage and current traces (a) and instantaneous power and energy traces (b) for a 30 cm long NS-DBD actuator driven at 10 Hz.

Figure 4 plots the coupled pulse energy (i.e. steady state energy) against the pulser operation time for different pulse repetition rates for a 46 cm long actuator. It can be seen that the pulse energy gradually increases with time before reaching a near steady state value after approximately 10 minutes. We note that time to reach the steady state is nearly independent of the pulse repetition rate, while the steady state pulse energy strongly depends on it. These results demonstrate that the energy coupled to the actuator is affected significantly by heating. We believe this is primarily due to heating of the plasma generator electronics. Details of this effect are beyond the scope of this paper.

Figure 5 illustrates the variation of the coupled pulse energy at steady state on the pulse repetition rate, at the conditions of Figure 4. It can be seen that increasing the pulse repetition rate from 10 Hz to 1 kHz results in coupled pulse energy increase by more than 50%, from 8.9 mJ to 14.8 mJ, but it is unclear if this energy increase is coupled to the near surface gas layer. This is likely due to the more filamentary behavior of the discharge at high frequency (see Figure 9), but no systematic studies have been undertaken to support this conjecture.
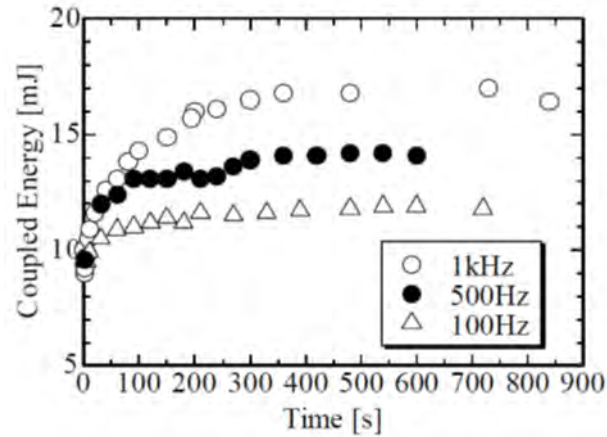
American Institute of Aeronautics and Astronautics

Figure 4. Coupled pulse energy vs. operation time for different pulse repetition rates for a 46 cm long actuator.
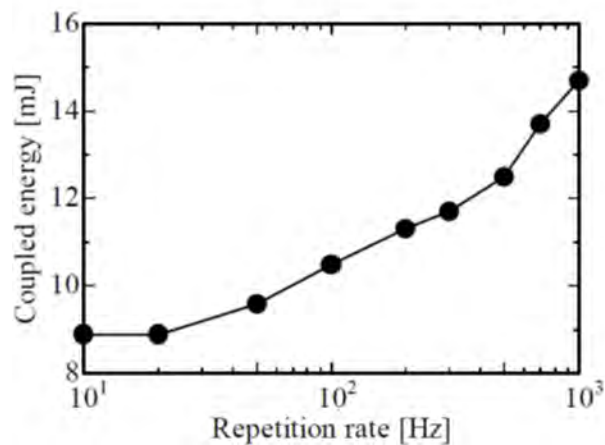

Figure 5. Coupled pulse energy at steady state vs. pulse repetition rate for a 46 cm long actuator.

B. Behavior in Quiescent Air

AC-DBD plasma actuator's control authority is shown to be primarily related to EHD interactions that produce tangential wall jets with maximum velocity of a few m/s.[31] The velocity field generated by the NS-DBD discharge in still air has been examined with PIV. Figure 6 presents ensemble-averaged velocity profiles for NS-DBD measured 20 mm downstream of the discharge for repetition frequency of 2 kHz. The actuator length in this case is 30 cm. An analogous AC-DBD induced velocity profile is shown for comparison. The two profiles are acquired using the same

American Institute of Aeronautics and Astronautics

actuator by changing the input waveform. A slight wall jet is generated by the NS-DBD actuator, but it is much weaker than the AC-DBD induced flow. Thus the EHD effect, while present for the NS-DBD plasma, is substantially weaker than in the case of AC-DBD. This very weak EHD effect has also been observed using smoke flow visualization for a shorter NS-DBD pulse width.[9] The limitations of low momentum AC-DBD plasma actuators are well-established.[32] This fact with the results of Figure 6 show that the EHD effects of NS-DBD are likely not a mechanism for flow control in the *Re* discussed in this work. Rather, rapid localized heating that excites natural flow instabilities is believed to be the source of control authority similar to that observed for LAFPAs in both experiments and computations. One of the characteristics of this control mechanism is the generation of compression waves due to rapid local heating of the near surface gas layer by the plasma. In the case of LAFPAs, these waves propagate spherically as if generated by point source.[15] Similar, but substantially more complex behavior has been confirmed for NS-DBD plasma using phase-averaged schlieren imaging.
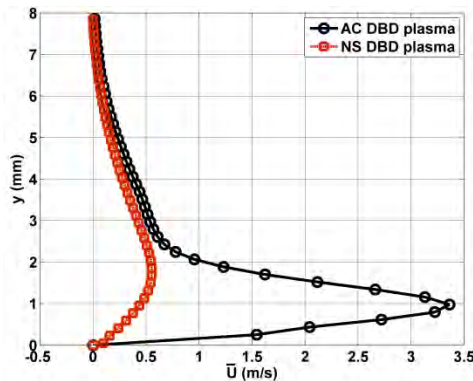

Figure 6. Mean velocity profiles for NS and AC-DBD plasma actuators operating in quiescent air at 2 kHz measured 20 mm downstream on a 30 cm DBD load.

Figure 7 shows phase-averaged schlieren images for three different time delays between the nanosecond discharge pulse and the schlieren light source (LED) pulse. Both the discharge and the schlieren light source pulse repetition rate is 1 kHz and the CMOS camera exposure time 156 msec (i.e. images are averaged over 156 discharge pulses). These images are taken using an actuator mounted on a cylinder, looking in the direction parallel to the cylinder axis. The surface of the actuator is curved in the image. The image visualizes the density gradient along the vertical axis and the second derivative of the density gradient along the horizontal axis. The intensity is

approximately proportional to the density gradient in the positive y-direction. Since the wave generated by the discharge pulse is propagating upward, a lower intensity indicates compression and a higher intensity indicates expansion. A wave system in Figure 7 consists of a compression wave and an expansion wave following it. To monitor the wave propagation, a series of schlieren images have been taken for delay times after the pulse ranging from 1 μsec to 50 μsec at 1 μsec intervals. The compression wave behavior is relatively complex as the wavefront is composed of both a quasi-planar and cylindrical compression wave, but appears relatively uniform along the viewing axis. This behavior is qualitatively similar to those reported by others in experimental and numerical results.[9,12]

Figure 7. Phase-averaged schlieren images of a compression wave generated by the nanosecond pulse discharge for several time delays after the discharge pulse.

Figure 8 shows phase-averaged schlieren images taken from a different direction, perpendicular to the cylinder axis. The cylinder is on the bottom of the images. In this orientation the line-of-sight averaged density gradient is considerably lower than in Figure 7, where it is averaged over the depth of field of approximately 10 cm. To combat this, the CMOS camera exposure time is increased and an additional filter was used to remove the discharge emission. Phase-avearged schlieren images in Figure 8 show a nearly plane wave front propagating along the vertical axis, as well as multiple circular waves. Similar to the images in Figure 7, higher signal intensity indicates compression and lower intensity indicates expansion. It can now be seen that the wave front near the actuator surface appears to have multiple ripples created by individual circular waves, coalescing into a superpositioned wave with an apparently plane front. It is likely that the line-of-sight averaging of these individual waves creates the circular wave front apparent in schlieren images of Figure 7. Since all schlieren images shown are averaged over

multiple discharge pulses, it appears that individual waves apparent in Figure 8 originate from relatively stable filaments which are repeatedly generated at nearly the same locations. This individual circular wave pattern correlates well with the discharge emission intensity pattern, providing additional evidence that some discharge filaments remain relatively steady pulse-to-pulse and thus generate repetitive waves, originating at nearly the same locations.[22] This can also be visualized using long exposure photographs. Various pulse repetition rates are shown in Figure 9. Camera exposure time is varied to keep the number of discharge pulses during the exposure approximately the same. DC input voltage 680 V and 300-320 discharge pulses are accumulated in each image. It can be seen that the discharge becomes progressively more filamentary as the pulse repetition rate is increased. At a pulse repetition rate of 100 Hz, the discharge appears diffuse and nearly uniform. However, as the repetition rate is increased above 1 kHz, multiple large-scale filaments begin to form. This correlates with the increased energy levels observed in Figure 4 and 5 at higher frequency. The filamentary nature of NS-DBD plasma has also been observed in ICCD images with nsec exposure time.[9,22] We postulate that the spatial location of the filament is a property of the actuator construction meaning two different actuators are not likely to develop these spatially stationary waves at the same location. These strong compression waves may be generated if the rate of localized heating in the filaments occurs on the time scale shorter than the acoustic time scale, $\tau_{acoustic} \sim d/a \sim 300$ nsec, where $d \sim 0.1$ mm is the filament diameter and $a \sim 300$ m/sec is the speed of sound. This rough calculation is supported by the employed pulse width (~100 ns).
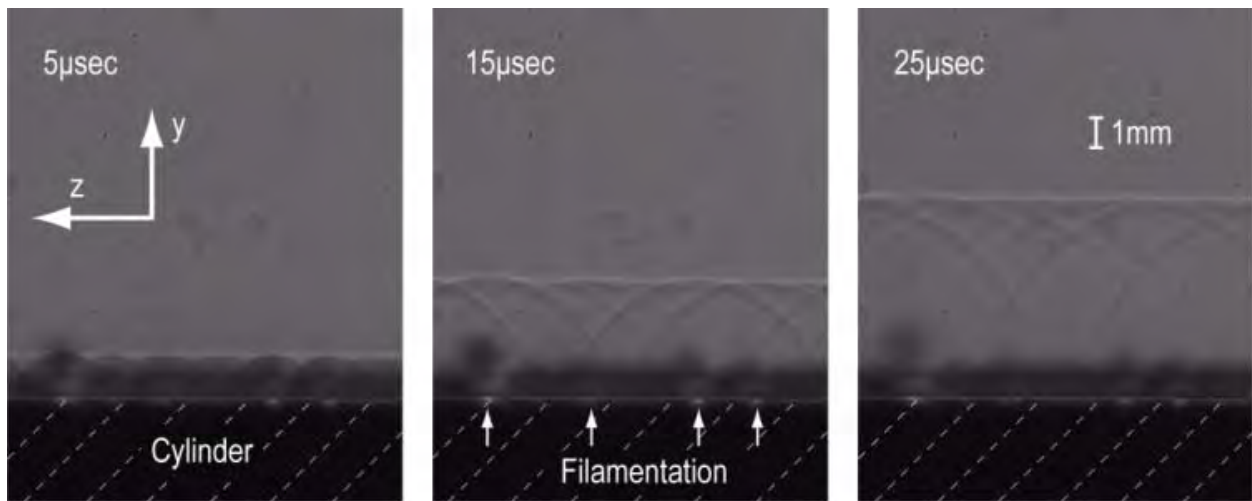

Figure 8. Phase-averaged schlieren images taken from a direction perpendicular to the cylinder axis.
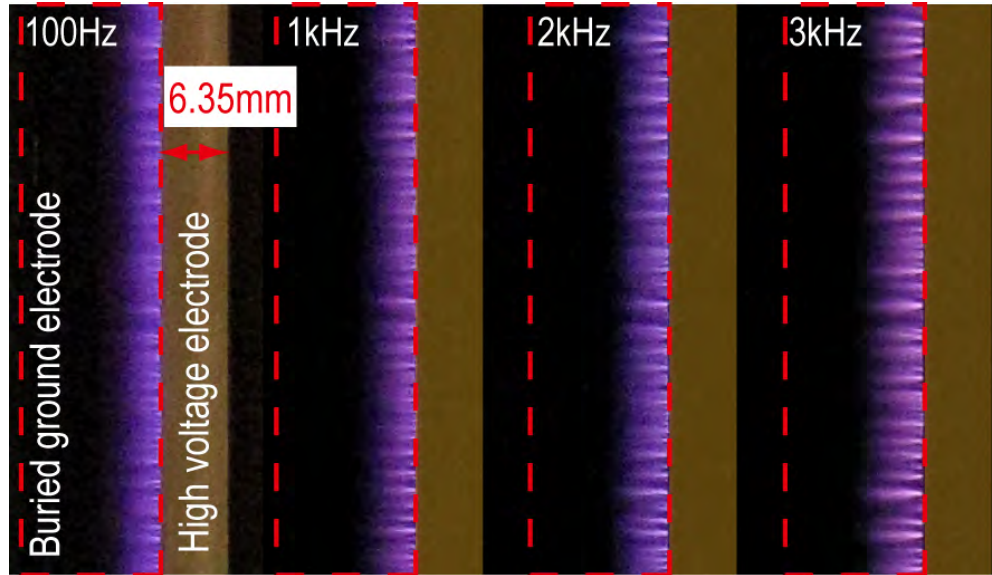
Figure 9. Photographs of a NS-DBD at different pulse repetition rates.

Figure 10 plots compression wave front position above the cylinder surface against the time delay between the nanosecond discharge pulse and the schlieren light source pulse. These data are obtained from the schlieren images of Figure 8. Compression wave front position is defined as the point where the schlieren signal intensity reaches a local maximum. Symbol size in Figure 10 indicates the uncertainty in the wave front location and schlieren light source timing. The trajectory of the M=1 sound wave at T=285 K (u=338 m/sec) is shown as a straight line for reference. One can see that a few mm from the cylinder surface, the speed of compression waves generated by the pulsed discharge (i.e. the trajectory slope) is approaching Mach 1. We postulate that the compression wave strength near the discharge may be greater as shown by Roupassov et al.[9], but better resolution is required to substantiate this claim. Clearly, more work is required to establish a full characterization for the amplitude of this device in terms of temperature or pressure difference across the wave. In any case, the production of this relatively weak compression wave is shown to have substantial effects on the flow field in Section IV. It should be noted that similar compression wave behavior does not exist in the literature for AC-DBD plasma actuators and thermal effects from these appear insignificant.[17-19]
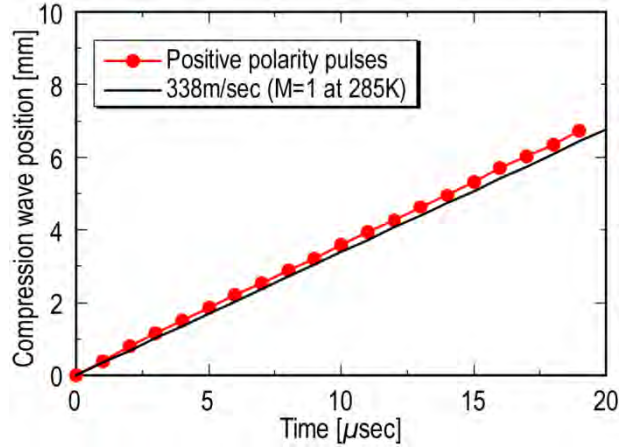
Figure 10. Time-resolved compression wave front location, inferred from the phase-averaged schlieren images.

IV. Flow Results

A. Airfoil Characterization

The $C_{L,max}$ angle for the NASA EET at Re=0.75 x10^6 is 12°.[23] The OSU version requires a boundary layer trip to perform in a similar fashion. Figure 11 compares NASA data with two OSU cases. The original airfoil with no trip installed has $C_{L,max}$ at 10 ^{o} with considerably different $dC_L/d\alpha$. Application of a boundary layer trip to the leading edge, in this case a passive DBD, corrects the $dC_L/d\alpha$ discrepancy and produces behavior more similar to NASA data. The stall characteristics are highly dependent on both the type and location of the tripping device as well as the wind tunnel flow quality. From this data, we conclude that the separating boundary layer is nominally laminar (or possibly transitional) at this Re. The offset in C_L values between the OSU and NASA models is primarily attributed to the lack of C_P resolution in the OSU case.
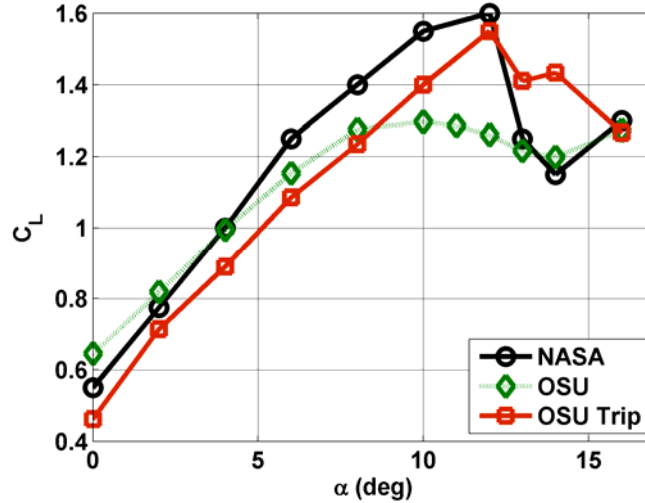
Figure 11: Comparison of C_L vs. α curves for NASA[23] and OSU EET airfoils for Re=0.75 x 10^6.

The focus of this work is on controlling separation at high α. This requires the actuator to be placed very near the leading edge ($x/c \approx 0$). The small scale model does not permit both a tripping device and a DBD actuator to be installed. The remainder of this work employs an actuator mounted slightly downstream of the leading edge (6 mm in arc length) with plasma formation in the upstream direction (Figure 12). The motivation for this is twofold. It places the location of plasma formation as close as possible to the expected separation line and eliminates any effect of the discontinuity from the high voltage electrode on the approaching boundary layer (i.e. the first surface discontinuity the flow encounters is the plasma side of the high voltage electrode). Additionally, the dielectric width is increased to 5.08 cm (2 inches) to move these surface discontinuities farther downstream (Figure 12). With this arrangement, as the flow travels from the stagnation point around the suction surface it encounters a discontinuity of 0.09 mm (3.5 mil) forward facing step, 0.09 mm (3.5 mil) backward facing step and lastly a 0.27 mm (10.5 mil) backward facing step (see curved arrow in Figure 12). Actuation (steady/unsteady blowing or AC-DBD) for leading edge separation control studies is usually introduced in the same direction as the mean flow. The reverse orientation is implemented with the assumption that the efficacy of thermal mechanisms for flow control is not directionally dependent. It should be noted that this orientation is also employed by Roupassov et al.[9]
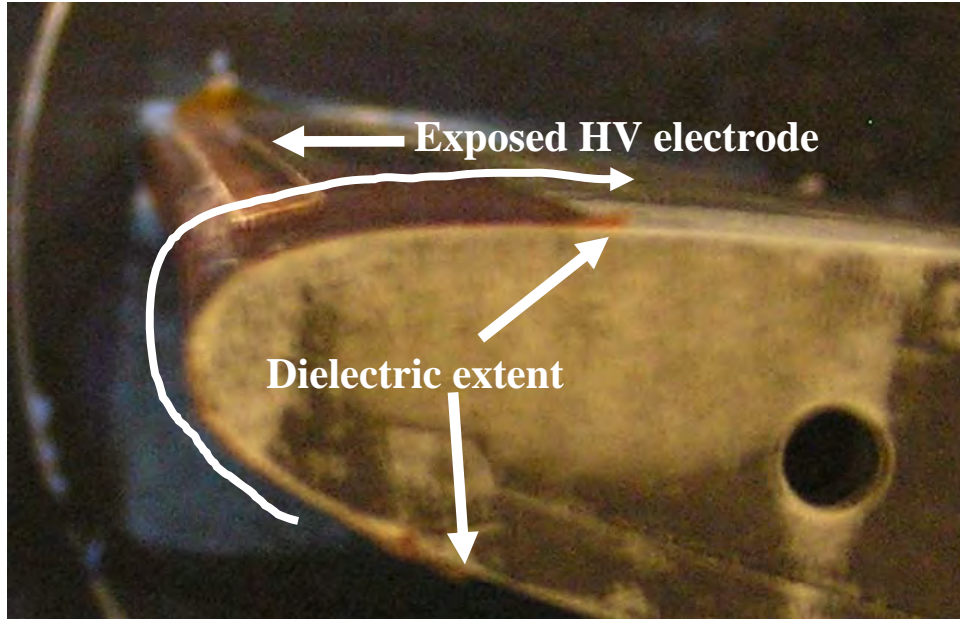
Figure 12: Photograph of the NS-DBD plasma actuator mounted near the airfoil leading edge in reverse arrangement (upstream edge located 6 mm in arc length from *x/c*=0).

Any reference to baseline conditions refers to the configuration where an actuator is mounted to the leading edge with no plasma generation. The C_L characteristics for this case are shown in Figure 13. The values are calculated by creating pin holes in the actuator at the location of pressure taps and integrating C_P. This effectively creates a short circuit and prevents plasma generation. The pre-stall performance is similar to the trip case in Figure 11, but the stall characteristics differ since this actuator is not as effective as a passive trip. NS-DBD plasma actuation is employed as an active trip at NASA pre-stall α (10-12°) in the following sections.
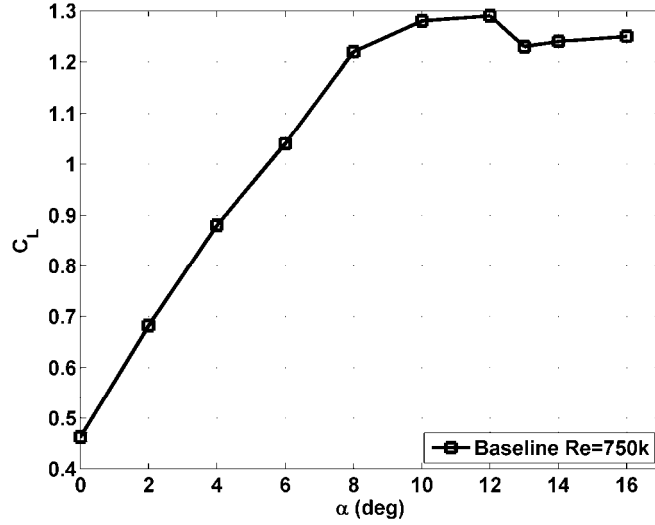
Figure 13: Baseline C_L vs. α data for Re=0.75 x 10^6.

High bandwidth pressure data from a transducer at x/c=0.40 at Re=0.75 x 10^6 are shown in Figure 14. The results are in general agreement with expectations from Figure 13. PSD magnitude begins to increase for α=10° consistent with the onset of stall. At higher α, the PSD magnitudes are further amplified consistent with full separation over the model. These data are provided to show there are no coherent dynamics associated with baseline separation although there is broad peak centered around F^+_c=2 at α=16°.
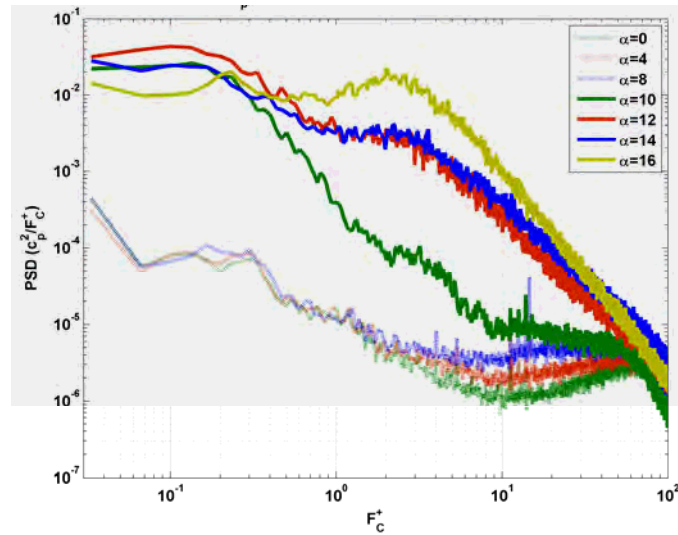

Figure 14: Baseline spectra of fluctuating pressure, c_p, measured at x/c=0.40 for Re=0.75 x 10^6 at various α.

B. Separation Control

An important aspect in leading edge airfoil separation control experiments is the physical mechanism by which control is achieved. Some examples for nominally 2D actuation include accelerating turbulent transition via an active trip, exciting spanwise vortices that entrain freestream momentum, and simply energizing the boundary layer through steady blowing allowing it to negotiate the severe adverse pressure gradient at the leading edge. The actuator characterization data for NS-DBD plasma (Figure 6) suggest the last one is not feasible at these Re. C_P and PIV data have confirmed the first two mechanisms can be accomplished up to Re=1 x 10^6 (62 m/s) depending on angle of attack and Re. This behavior has also been observed on a NACA 0015.[33]

Application of the actuator to the leading edge prevents measurements of static pressure in this region as seen in Figure 15a for both a stalled and attached condition. In lieu of ΔC_L, the change in C_P nearest the leading edge (which correlates with ΔC_L)[34] is employed (Figure 15a). Frequency sweeps using ΔC_P at x/c=0.05 as a metric are presented at Re=0.75 x 10^6 and 1 x 10^6 in Figure 15b. Three angles of attack are examined (12°, 14° and 16°) and each shows a different response to NS-DBD plasma actuation. It should be noted that the expected $C_{L,max}$ angle for this airfoil is 12° at these Re,[23] but the OSU version requires a boundary layer trip to perform in this fashion (see Figure 11). The data corresponding to this case (α=12°) in Figure 15 show no frequency preference in that once a threshold level is reached, control authority remains relatively constant. In the post-stall region beginning at α=14°, some optimal frequencies become apparent around F_c^+=4. As α is further increased, the preferred frequency increases up to a maximum of around 5.6 at α =16° while the control authority decreases. The control authority at α=16° has been reduced slightly in comparison to previous experiments.[34] This is expected result since the actuator is now likely aft of the optimal location for control (i.e. separation line) at α=16°. Despite this reduced control authority at high α, some significant flow physics are revealed. It is clear that the NS-DBD efficacy does not suffer due to the increased Re. In fact, in the two lower α cases, it is augmented. This is even more promising when considering that dynamic pressure, which is likely a more reliable scaling parameter than velocity or Re due to its direct relation to momentum, increases in proportion to U_∞^2. Note also that F_c^+ scaling holds quite well as the frequency preference for all three α is quite similar. It is also clear that there is some effect on the flow for all F_c^+ as the leading edge C_P value (x/c=0.05) has been improved by at least 0.5 in all cases. With this in mind, the flow physics in various frequency regimes is explored using PIV.
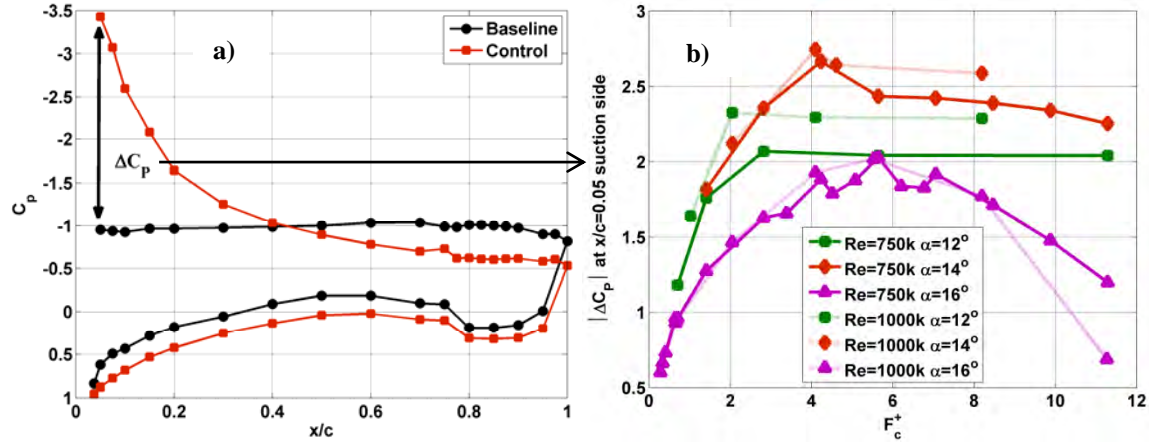
Figure 15: Effect of NS-DBD plasma on suction side C_P at x/c=0.05 as a function of F_c^+.

Figure 16a shows the NS-DBD plasma actuator effect on C_P for α=12°. This coincides with $C_{L,max}$ for the NASA airfoil and for the OSU model when a properly designed and placed trip can effectively attach the flow. The forcing frequency shown corresponds to a condition where the threshold frequency has been reached and further increases do not result in significant C_P improvement. The baseline flow is characterized by a weak adverse pressure gradient along the suction surface. This behavior is apparent in the ensemble-averaged vorticity field in Figure 16b as a strong region of vorticity signifies the boundary between the freestream and separated region over the model. Control at F_c^+=4 fully reattaches the flow creating a strong suction peak due to acceleration at the leading edge. It is also clear that stagnation point has moved downstream as expected. The ensemble-averaged vorticity field of Figure 16c shows stronger levels near the leading edge indicating a significant effect of the actuator on the flow in this region. Flow separation is observed near x/c=0.8 in both controlled pressure and vorticity data (Figure 16a,c).
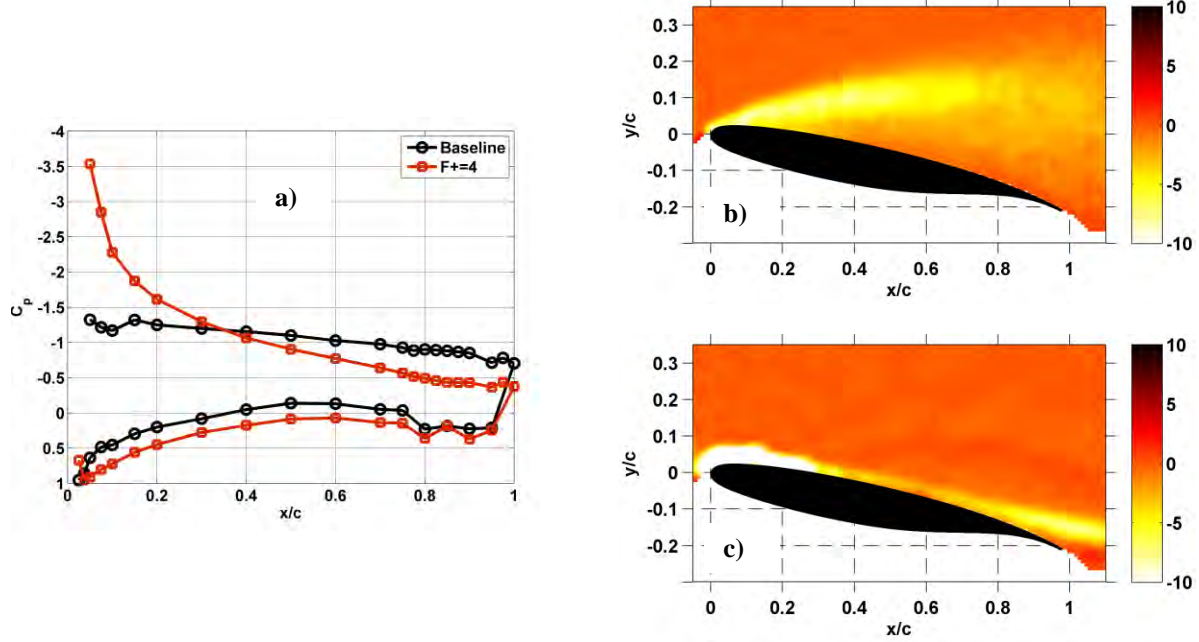
Figure 16. Time-averaged behavior of C_P (a) and normalized ensemble-averaged vorticity, Ω^*, for baseline (b) and NS-DBD forcing at $F_c^+=4$ (c) at $Re=0.75\times10^6$, $\alpha=12^o$.

Normalized swirling strength, $\lambda_{ci}^*=\lambda_{ci}c/U_\infty$, is employed for vortex identification in Figure 17. Unlike out-of-plane vorticity which identifies both rotation and shear, this technique ignores regions of pure shear and highlights regions of pure rotation.[35] The method is based on critical point analysis of the local velocity gradient tensor and its eigenvalues.[36] In two-dimensional form, the velocity gradient tensor is:

$$\nabla\tilde{W}=\begin{pmatrix}\dfrac{\partial\tilde{U}}{\partial x} & \dfrac{\partial\tilde{U}}{\partial y}\\[2mm]\dfrac{\partial\tilde{V}}{\partial x} & \dfrac{\partial\tilde{V}}{\partial y}\end{pmatrix} \tag{1}$$

where in this case the gradient has been applied to the phase-averaged velocity field, $\tilde{W}$. The parameter of interest is the imaginary component of the eigenvalues of Equation 2, which is nonzero only if:

$$\frac{\partial\tilde{U}}{\partial y}\frac{\partial\tilde{V}}{\partial x}-\frac{1}{2}\frac{\partial\tilde{U}}{\partial x}\frac{\partial\tilde{V}}{\partial y}+\frac{1}{4}\left[\left(\frac{\partial\tilde{U}}{\partial x}\right)^2+\left(\frac{\partial\tilde{V}}{\partial y}\right)^2\right]<0 \tag{2}$$

The imaginary component of the eigenvalues of Equation 2, λ_{ci}, is calculated using a 2nd order accurate central difference scheme and the normalized results are shown in Figure 17. Four phases ($\Delta\Phi=\pi/2$) of the actuation period are shown. None of the images show any recognizable dynamic content (i.e. coherent structures) although an effect of actuation very near the LE is apparent. There is also weak vortex formation aft of x/c=0.8, but the observable regions of swirl are mostly stationary. Thus, reattachment of the nominally separated flow does not occur through sustained production of large coherent structures in this case. Instead, the flow has been reattached through the use of the actuator as an active tripping device. This is supported by both NASA and OSU results (see Figure 11).
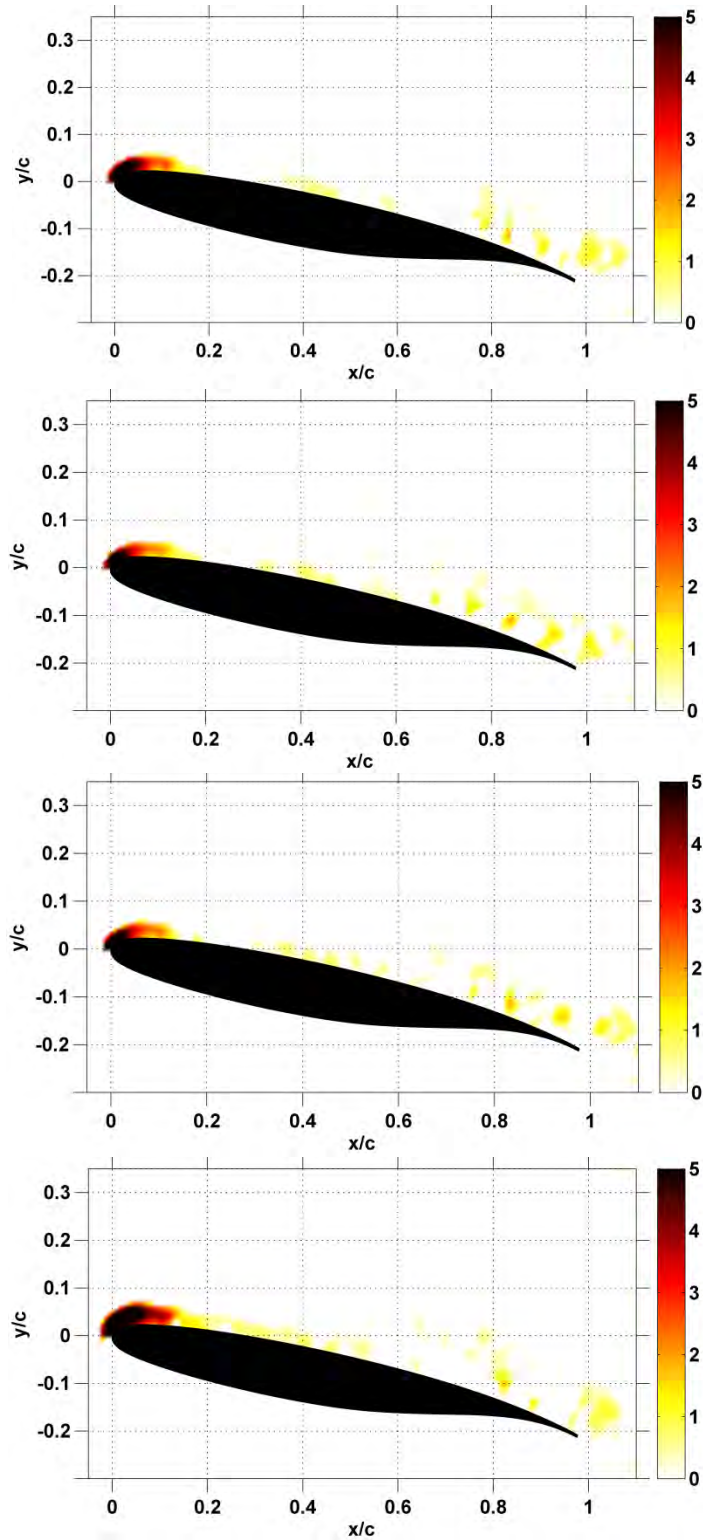
American Institute of Aeronautics and Astronautics

Figure 17 Phase-averaged ($\Delta\Phi{=}\pi/2$) **normalized swirling strength,** λ_{ci}^{*}**, for NS-DBD plasma forcing at** $F_c^{+}{=}4$ **at**

$Re{=}0.75\mathrm{x}10^{6}$**,** $\alpha{=}12^{\mathrm{o}}$**.**

Figure 18a shows the baseline and controlled C_P distributions for $\alpha=14^o$. In this case, the baseline is characterized by a zero pressure gradient stall with control effective in reattaching the separated flow along the suction surface to approximately 70% of chord. The ensemble-averaged normalized vorticity field shows this effect as the region of strong vorticity bounding the freestream and separated region is significantly more intense than the same figure for the $\alpha=12^o$ case (Figure 16b). Control moves the region of strong vorticity near the leading edge further upstream. This strong vorticity extends downstream to approximately $x/c=0.2$ after which a more diffuse region is observed (Figure 18c). Vorticity for this controlled case differs substantially from the $\alpha=12^o$ case. This can also be observed from the pressure data. The peak suction value and stagnation location are roughly equivalent to the $\alpha=12^o$ case, but further inspection reveals some important differences between the two pressure distributions. The value of C_P at $x/c=0.1$ in this case is approximately -2.6 compared to -2.3 in Figure 16a. Also, the average value of suction surface C_P from $x/c=0.7$-1.0 is -0.57 now where in Figure 16a it is -0.45. Note that the pressure surface C_P values are nearly equal between the controlled $\alpha=12^o$ and 14° cases except at 95% chord. With roughly equivalent C_P at the leading edge and along pressure surface, the decreased pressure along the suction surface predicts the C_L value should be greater in this case. However, one also expects the drag coefficient to increase in comparison given the suction surface pressure distribution beyond 70% chord which suggests a thicker downstream wake as indicated by the controlled vorticity fields.
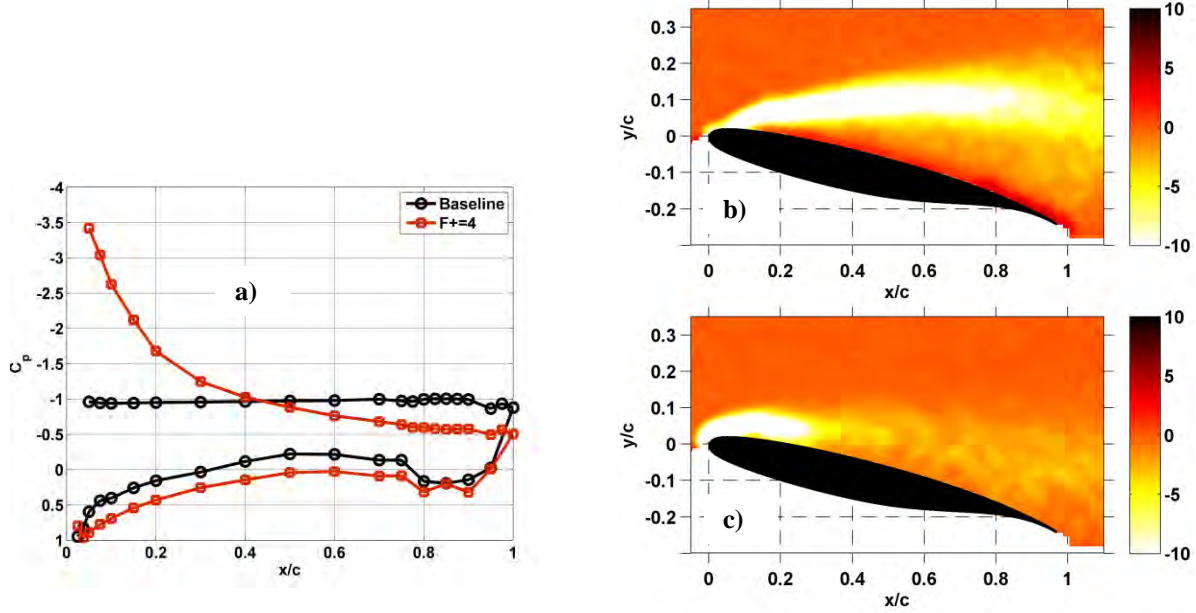
American Institute of Aeronautics and Astronautics

Figure 18. Time-averaged behavior of C_P (a) and normalized ensemble-averaged vorticity, Ω^*, for baseline (b) and NS-DBD forcing at $F_c^+=4$ (c) at $Re=0.75\mathrm{x}10^6$, $\alpha=14^o$.

The phase-averaged data sets in Figure 19 give the most striking description of the controlled flow field. Coherent structures dominate and the number of these structures is consistent with forcing at $F_c^+=4$. The effectiveness of these vortices for entraining freestream momentum and reattaching separated flows is well established in the literature.[37] Four phases of the actuation period ($\Delta\Phi=\pi/2$) clearly demonstrate the propagation of these organized regions along the airfoil chord. As expected, the coherent motion begins to break up further downstream ($x/c>0.65$). The dynamic content suggests that, in contrast to Figure 17, the control mechanism is not laminar to turbulent transition, but rather the excitation of flow instability through NS-DBD generated thermal perturbations. It also explains the variation in C_P between the $\alpha=12^o$ and 14° cases discussed previously as the flow fields are substantially different. This mechanism is well-established for separation control with oscillatory momentum injection, but to the authors knowledge this is the first evidence of such behavior using what we believe are primarily thermal perturbations. One also notes that the number of structures visualized over the chord is consistent with forcing at $F_c^+\approx4$. This confirms the belief that each NS-DBD pulse and its associated compression wave generates a coherent spanwise vortex in these conditions.
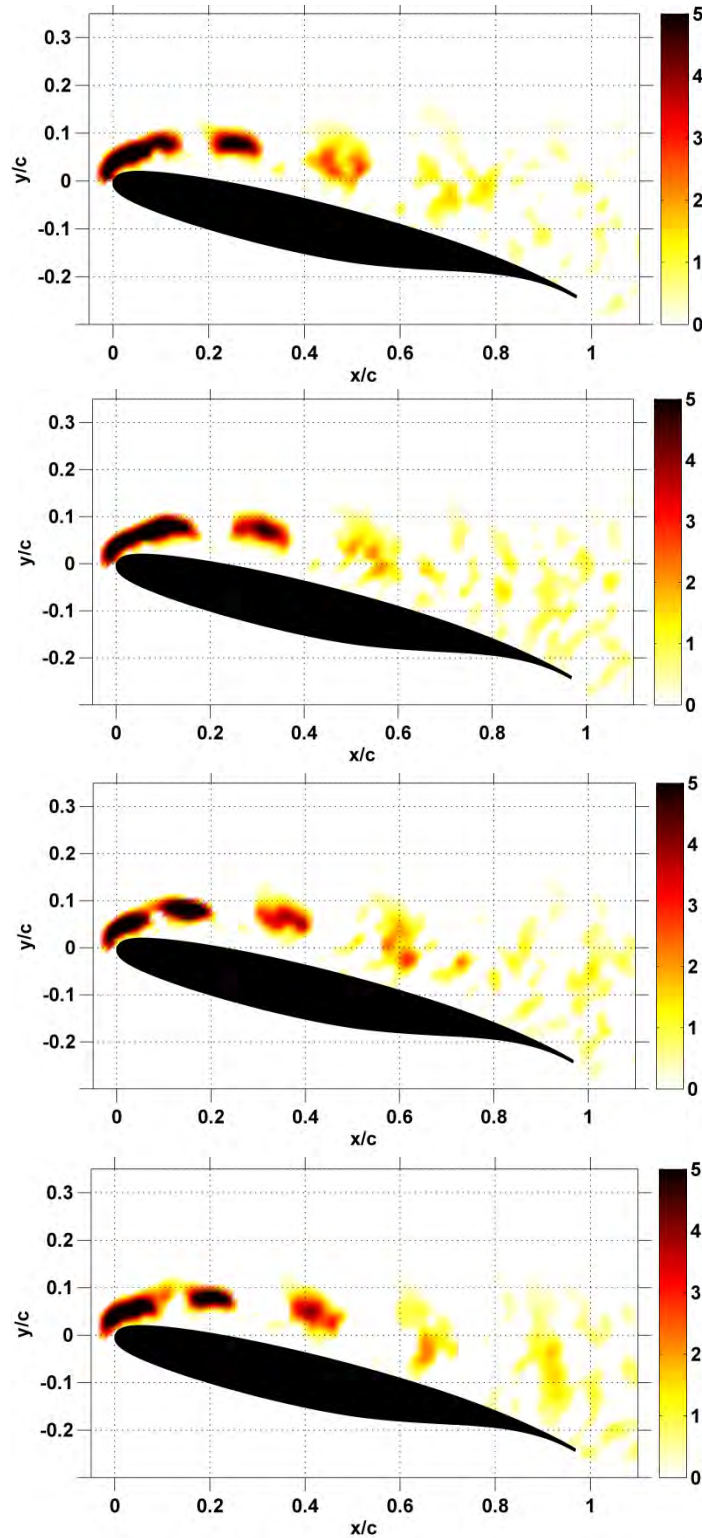
Figure 19 Phase-averaged ($\Delta\Phi=\pi/2$) **normalized swirling strength,** λ_{ci}^***, for NS-DBD plasma forcing at** $F_c^+=4$ **at** $Re=0.75\text{x}10^6$**,** $\alpha=14^\text{o}$**.**

American Institute of Aeronautics and Astronautics

The frequency preference indicated in Figure 15b for α=16° shows three relatively distinct forcing regimes. It should be noted that the optimal forcing frequency in this range (F_c^+=5.6) is greater than those normally encountered in such flow control studies (F_c^+~1). Some suggest a more appropriate length scale may be the projected length of the airfoil chord (csin(α)).[38] This is motivated by bluff body aerodynamics where for example the cylinder in cross flow is scaled by its diameter. This scaling renders flat plate airfoil frequency sweep data at various α self-similar under the pretext that the wake thickness is approximated by this simple projection. Indeed, this may provide scaling benefits and in the α=16° case, it would reduce the optimal F^+ to a value closer to those reported in the literature (F_c^+sin(α)=1.5). However, the common definition of F^+ is convenient for relating forcing frequency to the number of structures that exist over the separated region thus, we retain it here. It has been suggested that 1-4 vortices should exist over the controlled region, but the optimal F^+ is dependent on boundary layer state and forcing amplitude.[39]. Note that the reduction in efficiency often observed at higher F_c^+ is thought to be related to the smaller size of the generated vortices. Our data shows a slightly higher value (F_c^+=4-6) than usually observed, but it is unlikely that the thermal excitation mechanism is the cause of this discrepancy since the flow physics (i.e. production of spanwise vortices) are consistent with literature. This is supported by recent experiments on a NACA 0015 with NS-DBD that indicate optimal F^+ near 2.[33] Certainly, F^+≈1 provides guidance for selecting forcing frequencies, but is by no means a universal optimum.

Returning to the C_P and PIV data, low frequency forcing (F_c^+=0.6) has an effect on the naturally stalled flow as seen in the C_P curves, but in this case the minimum value is not observed nearest the leading edge (Figure 20a). Rather it appears further downstream near x/c=0.15. The ensemble-averaged vorticity certainly shows this change in behavior as the previously apparent shear layer is diffused considerably (Figure 20b,c). As before, the dynamic content of the flow is most compelling (Figure 21). In this low frequency case, regions of rotation are massively amplified in scale as they move over the model surface. Note that these structures do not follow the airfoil surface as closely as those shown in Figure 19. Instead, they are swept downstream by freestream momentum rather quickly once they move away from the leading edge. The magnitude of velocity fluctuations associated with this motion is approximately twice as large as similar data associated with Figure 19.[34] These massive coherent structures have been observed in all the low frequency forcing cases in Figure 15b. The vortex shedding associated with this low frequency forcing has also has strong audible signature which is associated with the vortex and not the plasma itself.
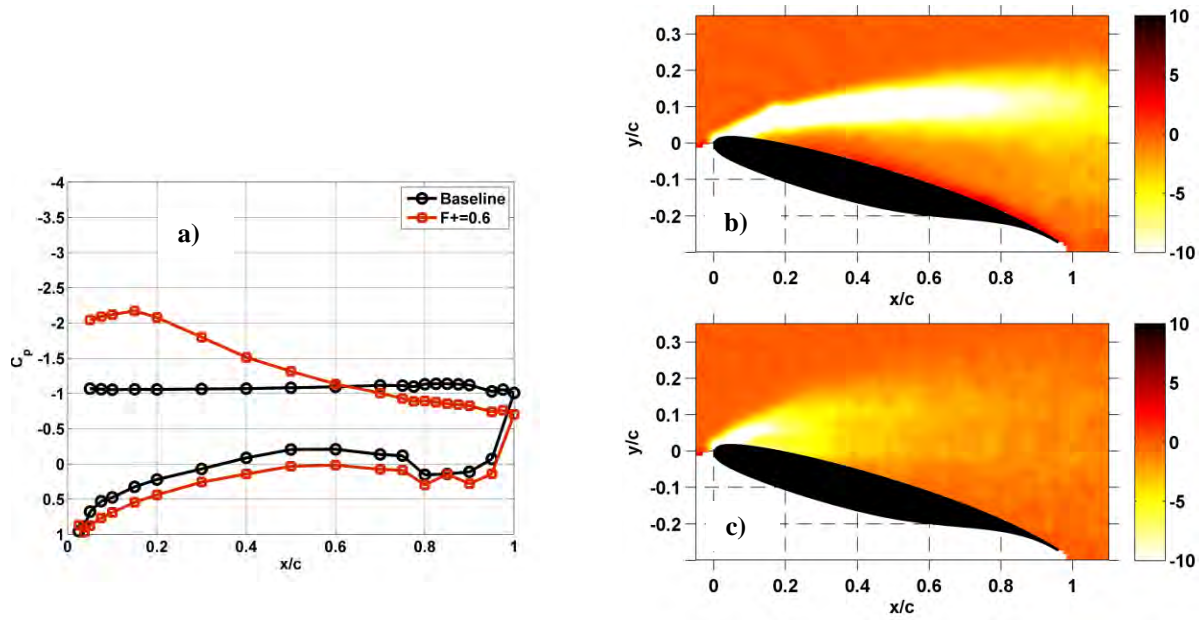
Figure 20. Time-averaged behavior of C_P (a) and normalized ensemble-averaged vorticity, Ω^*, for baseline (b) and NS-DBD forcing at $F_c^+=0.6$ (c) at $Re=0.75\times10^6$, $\alpha=16^o$
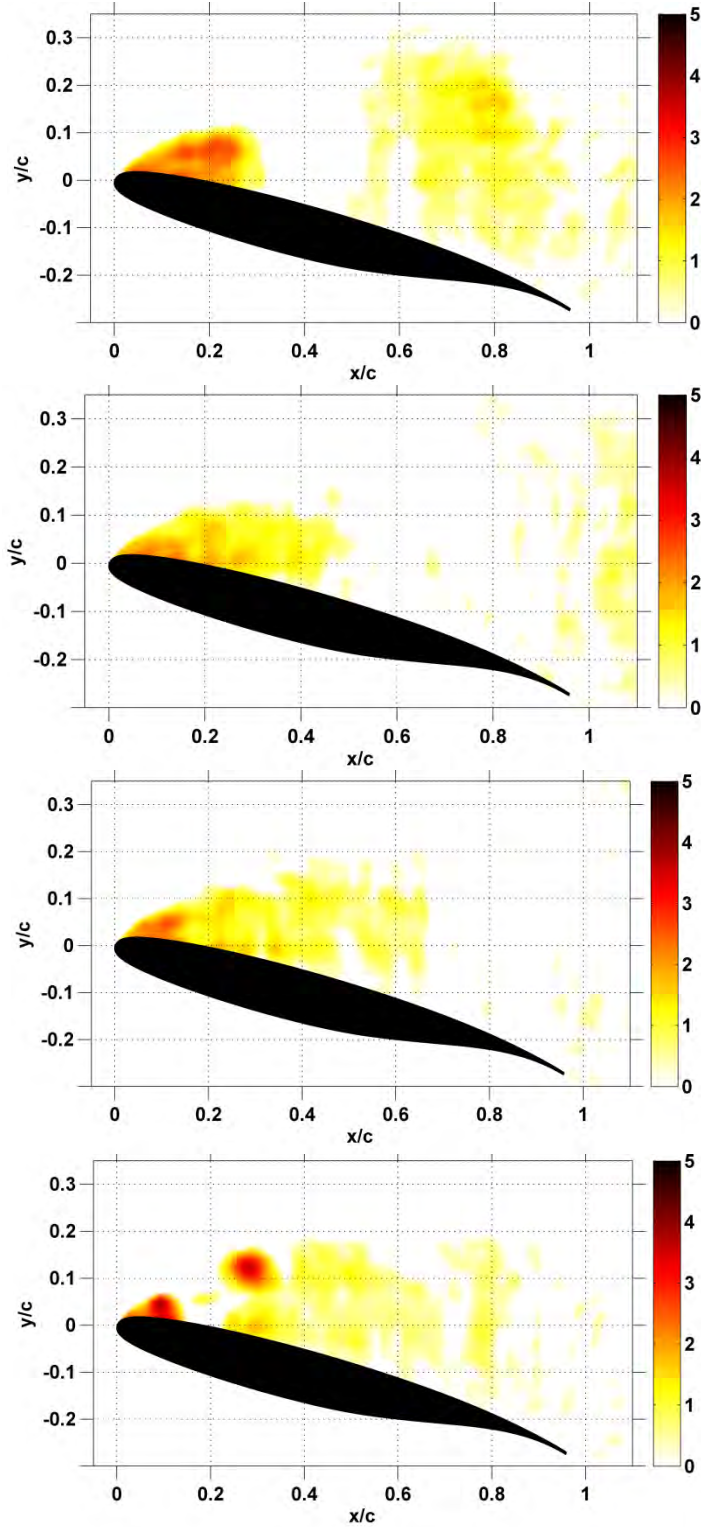
Figure 21 Phase-averaged ($\Delta\Phi=\pi/2$) **normalized swirling strength,** λ_{ci}^{*}, **for NS-DBD plasma forcing at** F_c^{+}=0.6 at Re=0.75x10^6, α=16°.

Optimal forcing (F_c^+=5.6) at α=16° produces reattachment over approximately half the model chord (Figure 22a). This can be identified by an adverse pressure gradient that exists up to x/c~0.6. The control authority in this case is diminished compared to optimal forcing at α=14° (Figure 18a) as the suction peak only reaches C_P=-3. The pressure side C_P is now slightly greater than observed in Figure 18a, but the value on the suction surface is considerably less with an average of -0.8 after x/c=0.4. This suggests that the C_L is still quite high, but C_D is becoming problematic due to a thicker wake. The ensemble-averaged vorticity further elucidates the effects of control. Forcing substantially changes the flow field as the intense shear layer over the entire model is eliminated (Figure 22b,c). However, evidence of thicker wake in comparison to Figure 18c is apparent as indicated from pressure data. The reduced control authority in this case is likely due to the movement of the separation line upstream resulting in a less than optimized position for the plasma actuator.
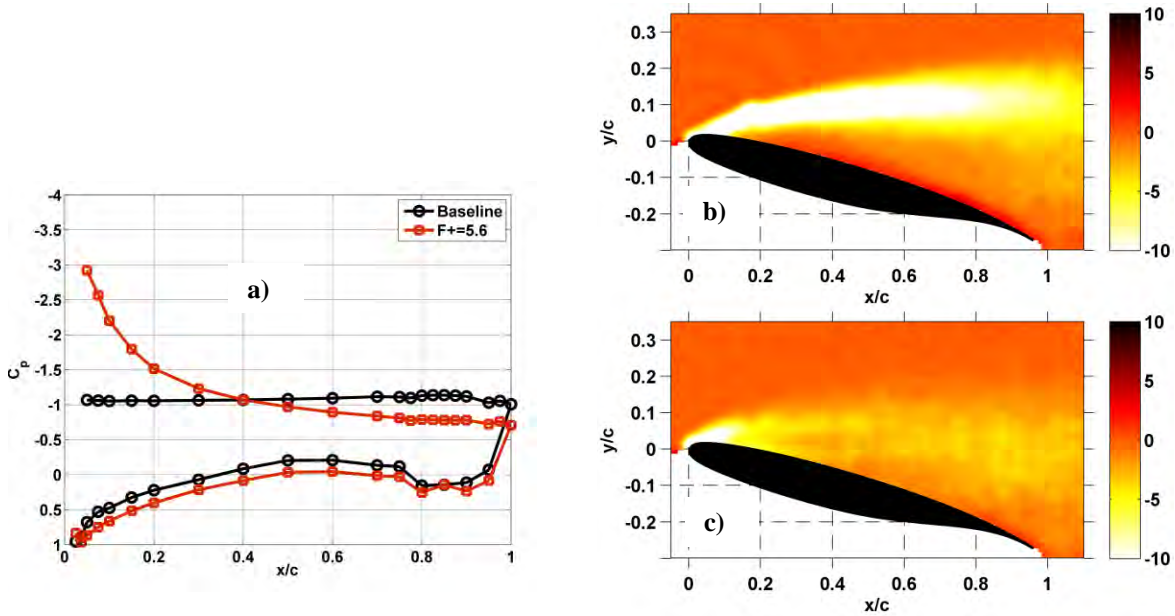

Figure 22. Time-averaged behavior of C_P (a) and normalized ensemble-averaged vorticity, Ω^*, for baseline (b) and NS-DBD forcing at F_c^+=5.6 (c) at Re=0.75x10^6, α=16°.

The phase-averaged velocity fluctuations again reveal clear dynamic content with scales indicative of forcing at F_c^+≈5.6. The coherent structures do not propagate as far downstream as those at α=14° before disintegrating. However, their organization near the leading edge is apparent in the phase-averaged swirling strength which shows clear vortex formation and convection near the leading edge (x/c<0.2) (Figure 23).
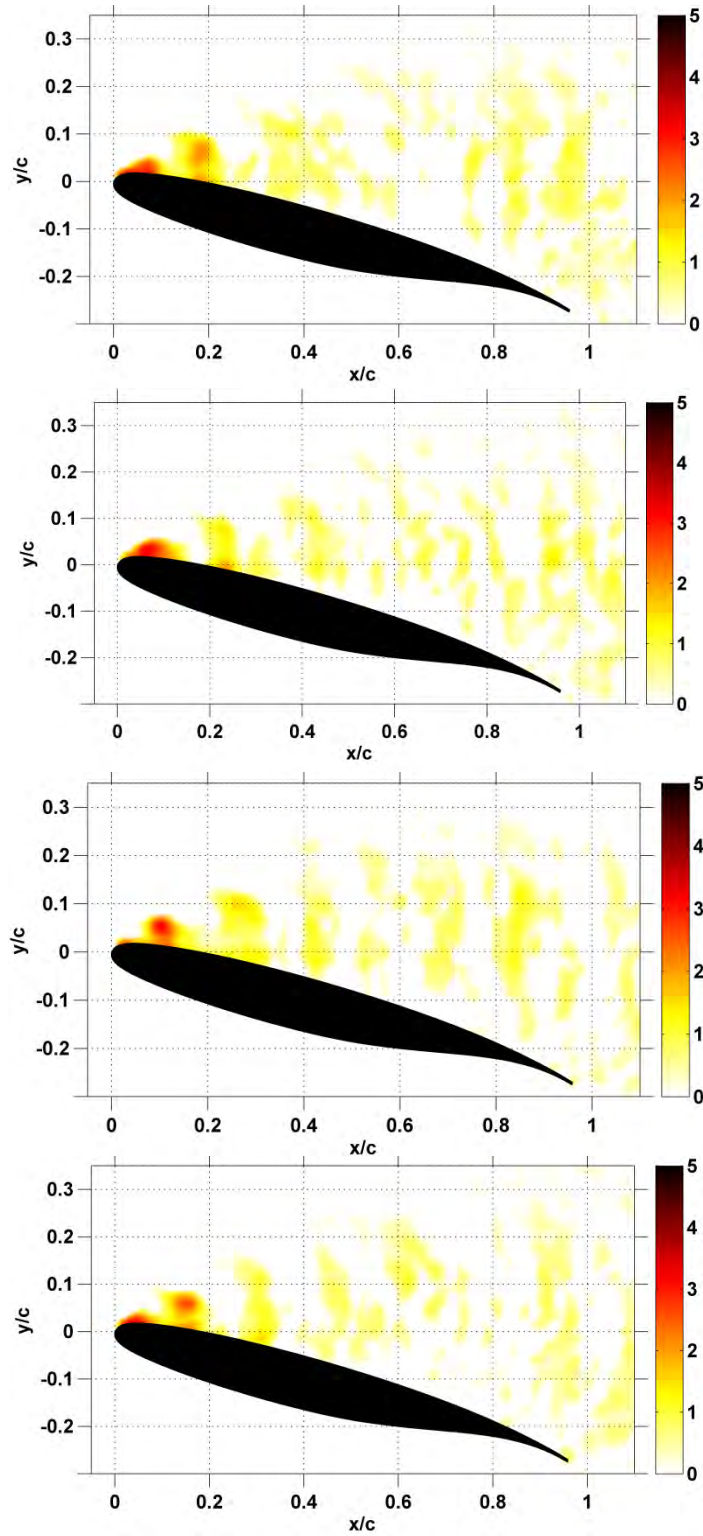
Figure 23 Phase-averaged ($\Delta\Phi=\pi/2$) **normalized swirling strength,** $\lambda_{ci}{}^{*}$**, for NS-DBD plasma forcing at** $F_c{}^{+}$**=5.6 at** Re**=0.75x10^6,** α**=16°.**

American Institute of Aeronautics and Astronautics

Finally the effects of high frequency forcing (F_c^+=11.3) are investigated. Although the leading edge C_P value is similar to the low frequency forcing case (Figure 20a), the form of the C_P curve just downstream of the leading edge suggests a very different flow field (Figure 24a). As in all cases, the ensemble-averaged vorticity is significantly altered by control (Figure 24b,c), but merely breaking up the intense shear layer over the airfoil is not sufficient to substantially reduce separation. The dynamic features are now much less apparent, but still exist near the leading edge (Figure 25) highlighting the robustness of the swirling strength metric. Despite the weak oscillations, distinct vortex formation and convection is identified at x/c<0.1 at a wavelength approximately half of that observed in Figure 23.
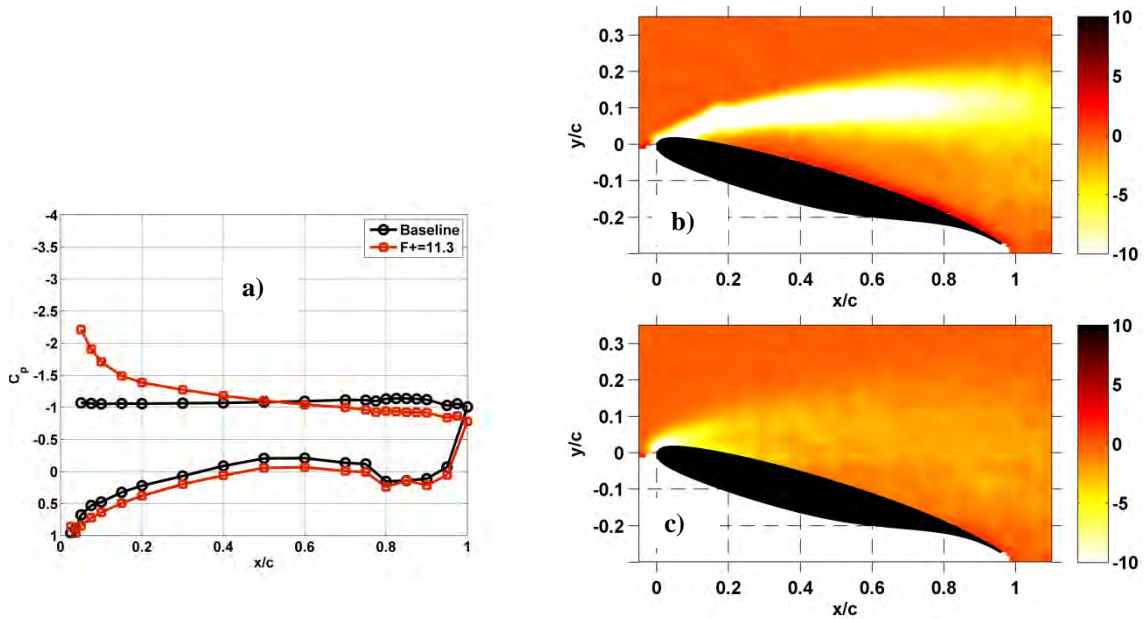

Figure 24. Time-averaged behavior of C_P (a) and normalized ensemble-averaged vorticity, Ω^*, for baseline (b) and NS-DBD forcing at F_c^+=11.3 (c) at Re=0.75x10^6, α=16°.
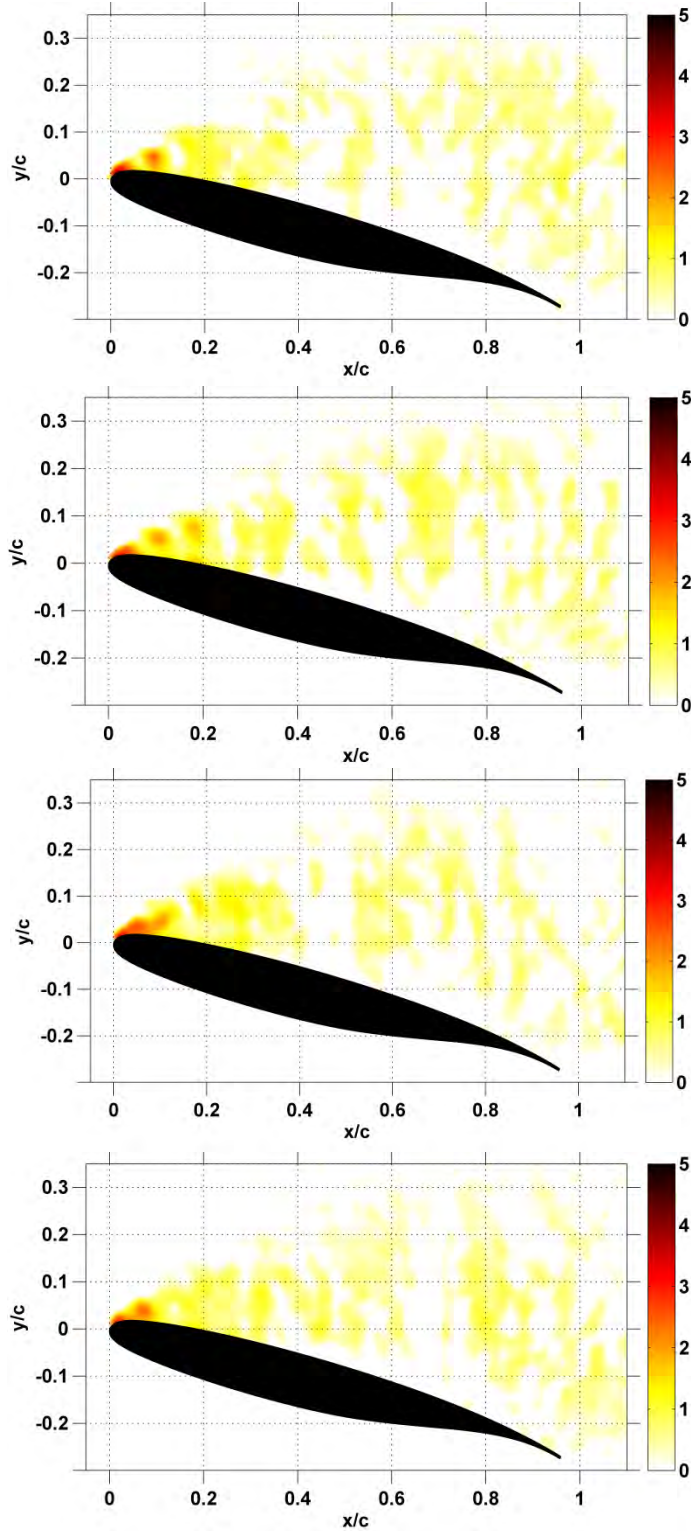
Figure 25 Phase-averaged ($\Delta\Phi=\pi/2$) **normalized swirling strength,** λ_{ci}^{*}, **for NS-DBD plasma forcing at** F_c^{+}**=11.3 at** Re**=0.75x10^6,** α**=16°.**

The preceding results for Re=0.75x10^6 have also been acquired at Re=1x10^6. As the results in Figure 15b indicate, the flow fields are quite similar in terms of control authority, ensemble-averaged and phase-averaged contents. The efficacy at which the NS-DBD plasma actuator excites coherent structures at the airfoil leading edge is particularly appealing. Although optimal frequencies exist for control, it seems that the NS-DBD possesses sufficient authority to manipulate flow instabilities and create structures at any frequency in the range of flow conditions surveyed. This is consistent with the high amplitude characteristics of LAFPAs.[13,15]

The C_L curve for the controlled cases is shown in Figure 26 as a final metric for demonstrating NS-DBD plasma actuator's capability. The baseline begins to stall around α=10° at Re=0.75x10^6 (45 m/s) and the NS-DBD plasma extends the stall angle up to 16°. The dimensionless excitation frequency at α=10° is 4. C_L values for α=12°, 14° and 16° have been calculated from the data in Figures 16, 18 and 22, respectively. Recall that C_P values near the leading edge are not measurable due to covering of the pressure taps by the actuator. Consequently, the C_L values have been estimated using the measured C_P values and linearly extrapolating the NS-DBD controlled data at the leading edge based on pre-stall values for a passive (no plasma) actuator modified to allow C_P measurements. This methodology is similar to other simplified C_L estimates,[40] but also employs the measured data away from the airfoil leading edge. The error bars on the figure are intentionally large due to the uncertainty introduced by this extrapolation. As suggested by previous data, the NS-DBD is capable of extending the stall angle to 16°, but we make no claims on the accuracy of the C_L values. Rather, the key result here is that in terms of stall angle only, the NS-DBD rivals the performance of a traditional passive control device (i.e. leading edge droop).[23]
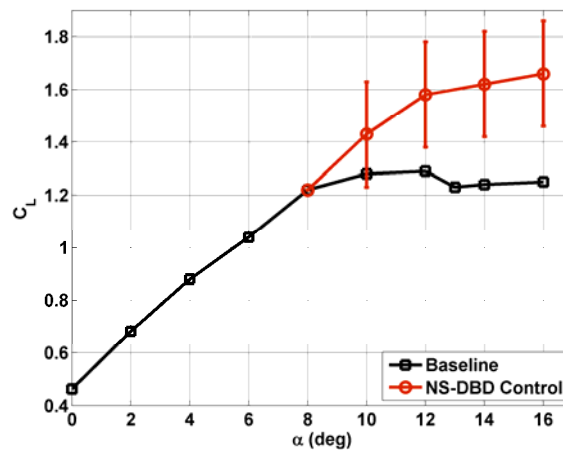

Figure 26: Effect of active control with NS-DBD plasma actuation on C_L for the OSU airfoil.

V. Discussion of Results

With details of the flow physics now presented, it is appropriate to return to the actuator characterization results for discussion of the connection between them. In Figure 4, a transient effect believed to be associated with heating of the pulser electronics is indicated. This transient phenomenon persists for approximately 10 minutes before reaching steady state. During this time, the coupled pulse energy is increasing. The data presented in Section IV have been acquired during the transient portion of the curve. For example, a set of PIV data requires ~75 seconds for acquisition (750 samples at 10 Hz). No obvious change in control authority is observed during a given experiment while monitoring C_P data at 1 Hz suggesting this transient has little effect on the flow control results, but these have not yet been extended past the 10 min interval. The degradation of an actuator will eventually play a role as run time and run frequency increase. A similar situation is found in Figure 5 which shows that the coupled energy increases with pulse repetition frequency. We postulate that this is due to the more filamentary behavior shown in Figure 9. At this time it is unclear if the increase in coupled energy results in increased heating of the near surface gas layer (and ultimately the strength of the compression wave) or merely heating of the actuator material. The data in Figure 15b do not show a similar correlation as that of Figure 9 as higher frequency does not result in more control authority and F_c^+ scaling is dominant. This is most strikingly depicted in Figure 21 where a relatively low frequency (~100 Hz) (i.e. low pulse energy) has a dramatic effect on the flow field. A calculation of the efficiency and amplitude characteristics of the device requires detailed near surface measurement of temperature rise and/or compression wave strength with and without the effects of freestream and efforts to this aim are ongoing.[22] In any case, it is clear that the velocity of the generated compression wave becomes approximately sonic a few mm from the discharge (Figure 10). It is perhaps surprising that these weak waves generate the high amplitude characteristics observed in Figure 20-25, but we note that similar wave speeds have been found in the case of LAFPAs[15] and higher near surface wave velocities for NS-DBD plasma have been suggested.[9,12]

The schlieren images of the Figure 8 show fairly complex 3D compression wave behavior, yet the flow physics reveal coherent spanwise vortices. These vortices are consistently generated for physically different actuators applied to the airfoil leading edge. Thus, the flat wave front found in the schlieren images in Figure 8 appears sufficient for producing spanwise vortices here. The 3D structure of the discharge and its effect on the flow are intended for future study. These results show compelling evidence for the use of repetitive nanosecond pulses applied to a DBD load for separation control. This generally supports the findings of Roupassov et al.[9] at takeoff and

landing velocities associated with typical transport aircraft although some distinctions can be made. The cited work employed shorter pulse width (~5-70 ns) and higher pulse voltage (25 kV) to guarantee the necessary heating in the near surface gas layer. The pulse width (~100 ns) and pulse voltage (~15 kV) employed in our work is sufficient to generate substantial control authority at the tested freestream conditions. It is probably no coincidence that the pulse energy between these two studies is of the same order of magnitude (~0.5 mJ/cm).

VI. Conclusions

The efficacy of repetitive nanosecond pulse driven dielectric barrier discharge (NS-DBD) plasma actuators for controlling flow separation from an airfoil leading edge has been demonstrated up to Re=1x10^6 (62 m/s). Results generally support the findings of Roupassov et al.[9] but the employed pulse parameters such as pulse width and peak voltage are less restrictive. The nanosecond pulse plasma generator used in this work has been custom designed and built in-house. The device has been characterized in quiescent air at atmospheric pressure. Current, voltage, instantaneous power and coupled pulse energy have been measured for different pulse peak voltages, pulse repetition rates, and actuator lengths. The results show that the actuator can be scaled to length of at least 1.5 m by simply increasing the DC supply voltage.[22] The coupled energy of the plasma is less than 1 mJ/pulse/cm in all cases (power <3 W/cm) which is sufficient for producing control authority in this work. This energy is dependent on both the run time and frequency of the discharge, but control authority does not show obvious dependence on coupled energy. Rather it obeys F^+ scaling, presumably because sufficient amplitude is produced even for low pulse energy.

The NS-DBD transfers substantially less momentum to the neutral air molecules than the more widely studied AC-DBD plasma actuator. The momentum transfer is quite weak and is not expected to have a significant effect in the flow in the conditions tested. Instead, the control authority generated by NS-DBD plasma is believed to stem from rapid localized heating of the near surface gas layer by the plasma. This gives rise to a complex pattern of quasi-planar and spherical compression waves in still air. Phase-averaged schlieren images suggest that some of these compression waves are generated by discharge filaments that remain fairly reproducible pulse-to-pulse. Despite the 3D behavior observed in quiescent air, a nominally 2D effect is observed on the airfoil leading edge as coherent spanwise vortices are developed. At nominally pre-stall angles of attack for high Re (α=12°), the NS-DBD

functions as an active trip while at post-stall it is found to manipulate flow instabilities to generate coherent spanwise vortices across the frequency range surveyed. The latter is widely recognized for controlling separation in a variety of flow systems. The device appears to possess high amplitude characteristics as structures are generated at all surveyed frequencies, but F_c^+ values in the range 4-6 are most effective for controlling flow separation. The control authority of NS-DBD does not suffer from Re effects between $Re=0.75\mathrm{x}10^6$ (45 m/s) and $Re=1\mathrm{x}10^6$ (62 m/s) and follows F_c^+ scaling as expected. At this time, the bandwidth of the device is limited to <3 kHz due to heating of the power supply, but there is no lower limit on pulse repetition frequency. Efforts to extend the operating frequency are ongoing. It should also be emphasized that burst mode of operation has not been employed and that each NS-DBD pulse is found to generate these large scale structures.

This work presents further evidence that the thermal mechanism observed in LAFPAs[13,15] and also presented by Roupassov et al.[9] can be employed for separation control with a DBD load. This may permit the use of DBD plasma actuators for high speed flow control applications ($Re>1\mathrm{x}10^6$, $U_\infty>100$ m/s) although the freestream conditions presented here must be extended to verify this hypothesis. Substantial work is also required to examine the effect of boundary layer state and thickness on NS-DBD control authority.

Acknowledgments

References

[1]Greenblatt, D. and Wygnanski, I., "The Control of Flow Separation by Periodic Excitation," *Progress in Aerospace Sciences*, Vol. 36, 2000, pp. 487-545.

[2]Seifert, A., Darabi, A. and Wygnanski, I., "Delay of Airfoil Stall by Periodic Excitation," *Journal of Aircraft*, Vol. 33, No. 4, 1996, pp. 691-698.

[3]Corke, T., Post, M. and Orlov, D., "Single Dielectric Barrier Discharge Plasma Enhanced Aerodynamics: Physics, Modeling and Applications," *Experiments in Fluids*, Vol. 46, 2009, pp. 1-26.

[4]Patel, M., Ng, T., Vasudevan, S., Corke, T., Post, M., McLaughlin, T. and Suchomel, C., "Scaling Effects of an Aerodynamic Plasma Actuator," *Journal of Aircraft*, Vol. 45, No. 1, 2008, pp. 223-236.

[5]Forte, M., Jolibois, J., Pons, J., Moreau, E., Touchard, G. and Cazalens, M., "Optimization of a Dielectric Barrier Discharge Actuator by Stationary and Non-Stationary Measurements of the Induced Flow Velocity: Application to Airflow Control," *Experiments in Fluids*, Vol. 43, 2007, pp. 917-928.

[6]Thomas, F., Corke, T., Igbal, M., Kozlov, A. and Schatzman, D., "Optimization of Dielectric Barrier Discharge Plasma Actuators for Active Aerodynamic Flow Control," *AIAA Journal*, Vol. 47, No. 9, 2009, pp. 2169-2178.

[7]Durscher, R. and Roy, S., "Novel Multi-Barrier Plasma Actuatos for Increased Thrust," AIAA Paper 2010-0965, 2010.

[8]Corke, T. C., Enloe, C. and Wilkinson, S. P., "Dielectric Barrier Discharge Plasma Actuators for Flow Control," *Annual Review of Fluid Mechanics*, Vol. 42, 2010, pp. 505-529.

[9]Roupassov, D., Nikipelov, A., Nudnova, M. and Starikovskii, A., "Flow Separation Control by Plasma Actuator with Nanosecond Pulsed-Periodic Discharge," *AIAA Journal*, Vol. 47, No. 1, 2009, pp. 168-185.

[10]Likhanskii, A., Shneider, M., Macheret, S. and Miles, R., "Modeling of Dielectric Barrier Discharge Plasma Actuator in Air," *Journal of Applied Physics*, Vol. 103, No. 053305, 2008, pp. 1-13.

[11]Opaits, D., Likhanskii, A., Neretti, G., Zaidi, S., Shneider, M., Miles, R. and Macheret, S., "Experimental Investigation of Dielectric Barrier Discharge Plasma Actuators driven by Repetitive High-Voltage Nanosecond Pulses with DC or Low Frequency Sinusoidal Bias," *Journal of Applied Physics*, Vol. 104, No. 043304, 2008, pp. 1-15.

[12]Unfer, T. and Boeuf, J., "Modelling of a Nanosecond Surface Discharge Actuator," *Journal of Physics D: Applied Physics*, Vol. 42, No. 194017, 2009, pp. 12.

[13]Samimy, M., Kim, J.-H., Kastner, J., Adamovich, I. and Utkin, Y., "Active Control of High-Speed and High-Reynolds-Number Jets using Plasma Actuators," *Journal of Fluid Mechanics*, Vol. 578, 2007, pp. 305-330.

[14]Kearney-Fischer, M., Kim, J.-H. and Samimy, M., "Control of a high Reynolds number Mach 0.9 heated jet using plasma actuators," *Physics of Fluids*, Vol. 21, 2009, pp. 095101.

[15]Samimy, M., Kim, J., Kearney-Fischer, M. and Sinha, A., "Acoustic and Flow Fields of an Excited High Reynolds Number Axisymmetric Supersonic Jet," *Journal of Fluid Mechanics*, Vol. 656, 2010, pp. 507-529.

[16]Gaitonde, D. and Samimy, M., " Coherent Structures in Plasma Actuator Controlled Supersonic Jets: Axisymmetric and Mixed Azimuthal Modes" to appear in *Physics of Fluids*, 2011.

[17]Jukes, T., Choi, K., Johnson, G. and Scott, S., "Characterization of Surface Plasma-Induced Wall Flows Through Velocity and Temperature Measurements," *AIAA Journal*, Vol. 44, No. 4, 2006, pp. 764-771.

[18]Sung, Y., Kim, W., Mungal, M. and Cappelli, M., "Aerodynamic Modification of Flow over Bluff Objects by Plasma Actuation," *Experiments in Fluids*, Vol. Vol. 41, 2006, pp. 479-486.

[19]Enloe, C., McLaughlin, T., VanDyken, R., Kachner, K., Jumper, E., Corke, T., Post, M. and Haddad, O., "Mechanisms and Responses of a Single Dielectric Barrier Plasma Actuator: Geometric Effects," *AIAA Journal*, Vol. 42, No. 3, 2004, pp. 595-604.

[20]Little, J. and Samimy, M., "High-Lift Airfoil Separation Control with Dielectric Barrier Discharge Plasma Actuation," *AIAA Journal*, Vol. 48, No. 12, 2010, pp. 2884-2898.

[21]Little, J., Nishihara, M., Adamovich, I. and Samimy, M., "High-Lift Airfoil Trailing Edge Separation Control Using a Single Dielectric Barrier Discharge Plasma Actuator," *Experiments in Fluids*, Vol. 48, 2010, pp. 521-537.

[22]Takashima, K., Zuzeek, Y., Lempert, W. and Adamovich, I., "Characterization of Nanosecond Pulse Dielectric Barrier Discharge Plasmas " AIAA Paper 2010-4764, 2010.

[23]Melton, L., Schaeffler, N., Yao, C.-S. and Seifert, A., "Active Control of Flow Separation from Supercritical Airfoil Leading-Edge Flap Shoulder," *Journal of Aircraft*, Vol. 42, No. 5, 2005, pp. 1142-1149.

[24]Melton, L., Yao, C.-S. and Seifert, A., "Active Control of Separation from the Flap of a Supercritical Airfoil," *AIAA Journal*, Vol. 44, No. 1, 2006, pp. 34-41.

[25]Melton, L., Schaeffler, N. and Lin, J., "High-Lift System for a Supercritical Airfoil: Simplified by Active Flow Control," AIAA Paper 2007-0707, 2007.

[26]Melton, L., Yao, C.-S. and Seifert, A., "Active Control of Separation from the Flap of a Supercritical Airfoil," AIAA Paper 2003-4005, 2003.

[27]Melton, L., Yao, C.-S. and Seifert, A., "Application of Excitation from Multiple Locations on a Simplified High-Lift System," AIAA Paper 2004-2324, 2004.

[28]Pack, L. G., Schaeffler, N. W., Yao., C. S. and Seifert, A., "Active Control of Separation from the Slat Shoulder of a Supercritical Airfoil," AIAA Paper 2002-3156, 2002.

[29]Benedict, L. and Gould, R., "Towards better uncertainty estimates for tublence statistics," *Experiments in Fluids*, Vol. 22, 1996, pp. 129-136.

American Institute of Aeronautics and Astronautics

[30]Opaits, D., Shneider, M. and Miles, R., "Electrodynamic Effects in Nanosecond-Pulse-Sustained Long Dielectric-Barrier-Discharge Plasma Actuators," *Applied Physics Letters*, Vol. 94, No. 061503, 2009, pp. 3.

[31]Moreau, E., "Airflow Control by Non-Thermal Plasma Actuators," *Journal of Physics D: Applied Physics*, Vol. 40, 2007, pp. 605-636.

[32]Mabe, J., Calkins, F., Wesley, B., Woszidlo, R., Taubert, L. and Wygnanski, I., "Single Dielectric Barrier Discharge Plasma Actuators for Improved Airfoil Performance," *Journal of Aircraft*, Vol. 46, No. 3, 2009, pp. 847-855.

[33]Rethmel, C., Little, J., Takashima, K., Sinha, A., Adamovich, I. and Samimy, M., "Flow Separation Control over an Airfoil with Nanosecond Pulse Driven DBD Plasma Actuators," AIAA Paper 2011-0487, 2011.

[34]Little, J., Takashima, K., Nishihara, M., Adamovich, I. and Samimy, M., "High Lift Airfoil Leading Edge Separation Control with Nanosecond Pulse Driven DBD Plasma Actuators " AIAA Paper 2010-4256, 2010.

[35]Little, J., "High-Lift Airfoil Separation Control with Dielectric Barrier Discharge Plasma Actuators," Ph.D. Dissertation, Mechanical Engineering, The Ohio State University, Columbus, OH, 2010.

[36]Adrian, R., Christensen, K. and Liu, Z., "Analysis and interpretation of instantaneous turbulent velocity fields," *Experiments in Fluids*, Vol. 29, 2000, pp. 275-290.

[37]Darabi, A. and Wygnanski, I., "Active Management of Naturally Separated Flow over a Solid Surface. Part 1. The Forced Reattachment Process," *Journal of Fluid Mechanics*, Vol. 510, 2004, pp. 105-129.

[38]Vey, S., Nayeri, C., Paschereit, C. and Greenblatt, D., "Leading Edge and Wing Tip Flow Control on Low Aspect Ratio Wings," AIAA Paper 2010.

[39]Seifert, A., Greenblatt, D. and Wygnanski, I., "Active Separation Control: An Overview of Reynolds and Mach numbers Effects," *Aerospace Science and Technology*, Vol. 8, 2004, pp. 569-582.

[40]Janiszewska, J. and Lee, J., "A Simple Method for Determining Lift and Drag on a Wing," AIAA Paper 2005-1061, 2005.